Deep-Sea Research Part I 141 (2018) 51–70

Contents lists available at ScienceDirect

Deep-Sea Research Part I

journal homepage: www.elsevier.com/locate/dsri

Biological and physical controls on the oxygen cycle in the Kuroshio Extension from an array of profiling floats

Seth M. Bushinsky[a,*], Steven R. Emerson[b]

[a] Atmospheric and Oceanic Sciences, Princeton University, USA
[b] School of Oceanography, University of Washington, USA

ARTICLE INFO

Keywords:
Argo profiling floats
Air-sea oxygen fluxes
Oxygen mass balance
Kuroshio Extension

ABSTRACT

The Kuroshio Extension (KE) is a current associated with the largest CO_2 flux into the Pacific Ocean, a broad region of uptake that extends across the Pacific basin between the subarctic and subtropical regions. The relative importance of the biological and physical processes controlling this sink is uncertain. Because oxygen is stoichiometrically linked to changes in dissolved inorganic carbon due to photosynthesis and respiration and subject to many of the same physical drivers as the CO_2 flux, in situ oxygen measurements help to determine the processes driving this large CO_2 flux. We analyzed data from eight Argo profiling floats equipped with oxygen sensors to estimate oxygen fluxes in the upper ocean of the KE region (approximate bounds: 25°N to 45°N, 135°E to 155°E). In situ air calibrations of these sensors allowed us to accurately measure air-sea oxygen differences, which largely control the flux of oxygen to and from the atmosphere. To characterize distinct biogeographical regions in the Kuroshio Extension and to accommodate seasonal north-south shifts in the location of the regional boundaries, we averaged oxygen measurements from different floats along isopycnal surfaces into 3 regions based on temperature-salinity relationships: North KE, Central KE, and South KE. Using these regional concentration time series, we determined the physical fluxes using an upper ocean layered model and calculated the residual oxygen flux, a combination of column-integrated net community production and physical processes unexplained by the model. The annual oxygen budget is largely a balance of air-sea exchange and the residual oxygen term. Residual oxygen fluxes are -5.4 ± 1.1, -5.9 ± 0.1, and 2.1 ± 2.2 mol O_2 m^{-2} yr^{-1} (where negative is a loss from the upper ocean) for the North, Central, and South KE regions, respectively. The North and Central KE are regions of mode water formation, which balances the large air-sea fluxes into the ocean. The South KE oxygen residual indicates a biologically produced flux to the atmosphere in two out of three years that agrees with previous estimates of subtropical annual net community production (ANCP) but exhibits high interannual variability. This study suggests that physical processes are the primary drivers for the annual uptake of the gases oxygen and carbon dioxide in the Central KE region where the annual CO_2 uptake is strongest.

1. Introduction

Over an annual cycle, the largest CO_2 flux into the northern Pacific ocean is found in the western Pacific, in and around the Kuroshio current and its extension into the North Pacific Transition Zone (NPTZ) (Takahashi et al., 2009, 2002) (Fig. 1). The Kuroshio brings warm water north, where it cools and mixes with nutrient rich waters, simultaneously increasing solubility and stimulating biological production. The Kuroshio Extension (KE) continues across the Pacific, dividing the subpolar Western Subarctic Gyre (WSG) from the North Pacific subtropical gyre to the south. The NPTZ occupies the region between the subtropical and subarctic frontal zones (Ayers and Lozier, 2012; Roden, 1991). The location of the Kuroshio Extension and its meanders varies seasonally and interannually (Jayne et al., 2009; Qiu and Chen, 2005), as does the NPTZ and its associated chlorophyll front (Ayers and Lozier, 2010; Bograd et al., 2004). The WSG is a high nutrient, low chlorophyll (HNLC) region that shows strong seasonal cycles in production (Harrison et al., 2004). In contrast, the subtropical gyre north of the equator is an oligotrophic region with on average a much smaller seasonal cycle in temperature and production (Nicholson et al., 2008). The Kuroshio Extension and the region to the north are also sites of mode water formation (Suga et al., 2008, 2004) where waters subduct into the subtropical gyre to the south.

The uptake of CO_2 is driven by solubility, biology, and mixing, with the importance of each process to the total CO_2 uptake a subject of ongoing research (Ayers and Lozier, 2012; Chierici et al., 2006; Palevsky

* Corresponding author.
E-mail address: sb17@princeton.edu (S.M. Bushinsky).

https://doi.org/10.1016/j.dsr.2018.09.005
Received 7 January 2018; Received in revised form 15 September 2018; Accepted 16 September 2018
Available online 18 September 2018
0967-0637/

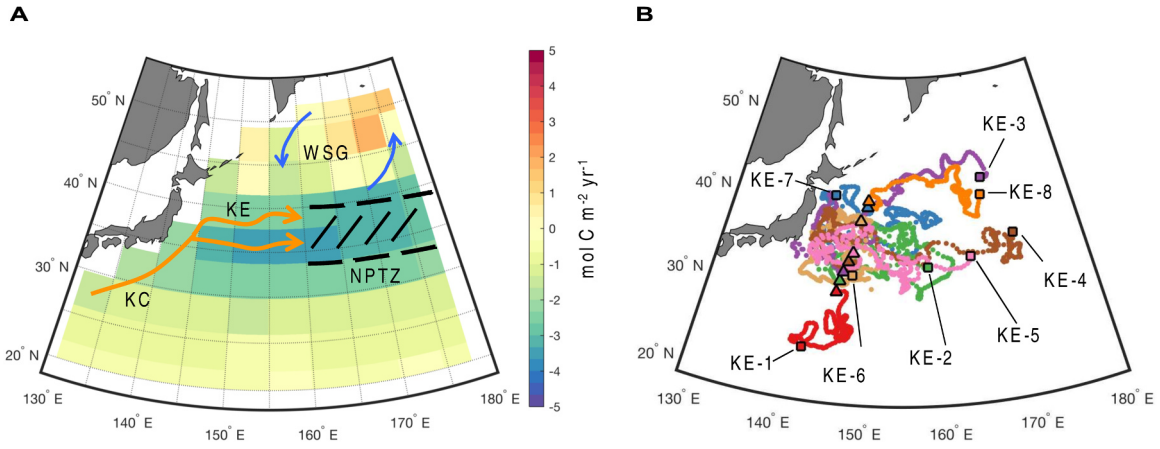

Fig. 1. (A) Important currents near float locations in the Pacific and air-sea carbon fluxes (Takahashi et al., 2009). In the western Pacific, the Kuroshio Current (KC) brings warm water north into the Kuroshio Extension (KE), where it cools and continues into the North Pacific Transition Zone (NPTZ). The NPTZ is an area of enhanced chlorophyll and productivity that separates the subarctic Western Subarctic Gyre (WSG) from the North Subtropical Gyre. The location of the KE and NPTZ vary on seasonal and interannual timescales. Gridded air-sea fluxes of carbon dioxide shown by the colors (Takahashi et al., 2009) indicate a large annual flux of carbon dioxide into the ocean associated with the KE and NPTZ. Currents and water mass locations from: Ayers and Lozier (2010), Chierici et al. (2006), Harrison et al. (2004), Hayward (1997), Roden (1991), Wakita et al. (2016). (B) Float tracks (right panel) for the entire deployment lifetimes of the SOS-Argo floats used in this study. Triangles represent deployment locations and squares indicate final float positions. (For interpretation of the references to colour in this figure legend, the reader is referred to the web version of this article).

and Quay, 2017; Takahashi et al., 2002). Strong temporal variability in the physical drivers of gas flux, temperature, and winds, plus changes in biological parameters such as light and nutrient availability, produce large seasonal variations in the strength of the CO_2 flux (Takahashi et al., 2009). Spatial heterogeneity of water mass properties creates distinct ecological regions. Longhurst et al. (1995) divided the Pacific north of the NPTZ into ecological domains based on nutrient supply, further subdividing these domains into biogeochemical provinces defined by physical parameters. More recent studies have worked to characterize the boundaries of regions in the North Pacific based on sea surface temperature (SST) and nitrate gradients (Wong et al., 2002) or persistent patterns of satellite-derived chlorophyll (Hardman-Mountford et al., 2008) and determine their biogeochemical characteristics and properties.

Determining the processes driving CO_2 exchange in the Pacific Ocean is difficult given the spatial and temporal scales involved. Time series sites equipped to undertake detailed process studies are often confined to a small physical area while the CO_2 uptake in the North Pacific is spread over much of the basin. Takahashi et al. (2002) determined the magnitude of CO_2 flux caused by seasonal temperature-induced solubility changes and attributed the remainder of the observed CO_2 uptake to biological export. This method indicates that both temperature and biological effects are strong throughout the region north and south of the Kuroshio Extension, with biology dominating to the north where the subpolar water mixes into the Kuroshio Extension and temperature dominating to the south. It is important to note in Takahashi et al. (2002) that physical terms such as mixing are included in the biological term. Ayers and Lozier (2012) modeled physical controls on the NPTZ and found that biology and geostrophic advection of low dissolved inorganic carbon (DIC) waters were of approximately equal importance to the total CO_2 flux. However, because the flow of the Kuroshio from south to north cools the water, driving an influx of CO_2, this physical mechanism is still fundamentally a solubility driven pump, though different than the seasonal cycle in temperature at a fixed physical location.

In a pair of papers, Palevsky et al. (2016) and Palevsky and Quay (2017) calculated a small positive, though not significantly different from zero, annual net community production (ANCP) in the Western Pacific of 0.5 ± 0.7 mol C m^{-2} yr^{-1} from O_2/Ar measurements made on ships of opportunity. Furthermore, they calculated that the overall contribution of ANCP to the DIC budget was equally small, yet still had an impact on the air-sea flux of CO_2 due to the slow exchange rate of CO_2 and the shallow mixed layer during the summer when production occurs.

Oxygen measurements can be used to determine biological carbon export (Bushinsky and Emerson, 2015; Emerson et al., 2008; Emerson and Stump, 2010). The amount of oxygen produced during photosynthesis can be related to the amount of organic carbon fixed through a stoichiometric ratio that is, on average, 1.45 O_2/C_{org} (Hedges et al., 2002). Over an annual cycle, and assuming no net physical inputs, any oxygen produced during photosynthesis but not consumed by respiration is related to the amount of organic carbon fixed that was removed from the upper ocean as part of the biological carbon pump (Volk and Hoffert, 1985). In general, the signs of the net air-sea oxygen and CO_2 exchange depend on the forcing mechanism: net biological production produces an oxygen flux to the atmosphere and a CO_2 flux into the ocean; solubility changes induced by temperature seasonality create air-sea O_2 and CO_2 fluxes in the same direction; and exchange with deeper waters brings O_2-poor and CO_2-rich waters to the mixed layer, creating disequilibria with the atmosphere that drives an oxygen flux to the ocean and CO_2 flux to the atmosphere.

The recent deployment of Argo profiling floats equipped with oxygen sensors has greatly expanded the availability of in situ oxygen measurements over annual cycles (Gruber et al., 2009). Initially, poor analytical accuracy hampered the calculation of air-sea oxygen fluxes, which are primarily a function of the concentration difference from saturation equilibrium with the atmosphere. Recent advances in calibration of these oxygen sensors against the atmosphere (Bittig et al., 2017; Bittig and Körtzinger, 2016, 2015; Bushinsky et al., 2016; Emerson and Bushinsky, 2014; Johnson et al., 2015) now provide accuracies in concentration of better than ± 0.5% and in air-sea concentration difference of about ± 0.25%. Uncertainties in the wind-speed dependent air-sea gas exchange rate parameterization have been another hurdle for determining air-sea oxygen fluxes from surface oxygen measurements. However, recent advances in parameterization of the bubble mechanisms of the air-sea flux (Liang et al., 2013) and subsequent tuning to surface ocean N_2 measurements (Yang et al., 2017) have greatly improved the models of air-sea oxygen exchange. Advances in both in situ oxygen measurements and the models of air-sea exchange have made it possible to interpret float oxygen measurements in terms of the biological and physical processes. While many studies have used oxygen equipped Argo floats individually or for

sub-surface applications, to our knowledge only a few studies have previously made use of groups of oxygen equipped Argo floats to understand biogeochemical processes in the surface ocean: a study at Ocean Station Papa in the Gulf of Alaska that used multiple deployments as a multi-year time series (Plant et al., 2016), a study looking at biogeochemical responses to high-resolution forcing in the Kuroshio region (Inoue et al., 2016a, 2016b), a study in the Southern Ocean looking at bulk air-sea oxygen exchange (Bushinsky et al., 2017), and one in the Labrador Sea that characterized oxygen saturation during deep water formation events (Wolf et al., 2018).

In this study we define three regions of the Kuroshio Extension with distinct seasonal cycles of the oxygen saturation anomaly using temperature and salinity relationships. We average oxygen concentrations from eight floats along isopycnal surfaces within each region and use an upper ocean multi-layer model to understand the physical and biological fluxes that contribute to the observed oxygen concentrations. The goal of this study is to add to our conceptual understanding of the biological and physical drivers of the strong air-sea flux of carbon into the ocean in this region and demonstrate procedures for large-scale interpretation of biogeochemical Argo measurements.

2. Methods

2.1. Special Oxygen Sensor (SOS)-Argo Float Deployments

The Argo array primarily consists of ~3800 profiling drifters that measure temperature, salinity, and pressure in the upper 2000 m of the water column. These floats profile every 10 days, parking at 1000 m after each profile. Oxygen and other biogeochemical sensors are increasingly being added to Argo floats (Gruber et al., 2009; Johnson et al., 2017). Argo floats used in this study (Special Oxygen Sensor: SOS-Argo) are modified APEX floats developed at the University of Washington designed to allow in situ atmospheric calibration of the oxygen optodes (Bushinsky et al., 2016; Bushinsky and Emerson, 2015; Emerson and Bushinsky, 2014). The oxygen optodes (Aanderaa model 4330) are raised on 60 cm stalks to facilitate atmospheric measurements of the partial pressure of oxygen (pO_2) while at the surface with minimal interference from surface waves and splashing. Oxygen optodes are known to drift significantly prior to deployment at surface temperatures and pressures (Bittig and Körtzinger, 2015; Bushinsky and Emerson, 2013; D'Asaro and McNeil, 2013; Johnson et al., 2015; Takeshita et al., 2013) and recent evidence indicates the presence of a smaller, but still significant drift after deployment (Bittig et al., 2017; Bittig and Körtzinger, 2016; Bushinsky et al., 2016; Bushinsky and Emerson, 2015; Drucker and Riser, 2016). Atmospheric measurements after each ocean profile provide a long-term calibration to correct for drift, both prior to deployment and during float operation.

Eight floats were deployed south of, in, and north of the Kuroshio Extension along a track from 30° to 40°N in March 2013 (Fig. 1, Table 1) and operated on 5–10 day cycles until late 2016 when their batteries died. The floats drifted over a large area, completing 2083 profiles (~260 per float) while staying roughly within the region of carbon uptake associated with the Kuroshio Extension. Floats were deployed from south to north and are named according to their deployment order (KE-1 at 30°N, 146.4°E to KE-8 at 40.5°N, 149.7°E; Table 1). In this paper we refer to the broader region from ~25°N to ~45°N and ~135°E to ~155°E as the Kuroshio Extension region, or KE.

2.2. Calibration of oxygen sensors

Aanderaa oxygen sensors used in this study were calibrated against Winkler oxygen measurements at 5 different oxygen concentrations and 5 different temperatures in the laboratory before deployment as described in Bushinsky et al. (2016). After deployment, the SOS-Argo oxygen optodes were repeatedly calibrated against atmospheric measurements. At the end of each profile, 30 air samples were taken over a one-hour period. These atmospheric measurements were compared to expected atmospheric pO_2 based on reanalysis pressure and humidity data from the National Centers for Environmental Prediction (NCEP). Initial calibration and subsequent drift corrections were based on a linear fit to the offset between measured and expected atmospheric pO_2 (see Bushinsky et al., 2016, for more details). The analysis of Bittig et al. (2017) suggests that artifacts can be present in atmospheric calibration at different temperatures over the course of a 3–4 year deployment due to an incomplete characterization of the temperature sensitivity of the optode response during the batch "factory calibration". We avoid these issues through our additional laboratory calibration of individual optodes. Three of the optodes displayed a negative drift (loss of sensitivity) averaging -0.3% yr^{-1}, three did not drift significantly, and two indicated a positive drift of 0.2% yr^{-1} (Bushinsky et al., 2016).

3. Results

Examples of float measurements of temperature, oxygen, O_2 saturation anomaly, and mixed layer depth from float KE-3 are plotted in Fig. 2 (data from the other 7 floats are in Appendix A). Oxygen saturation anomaly ($\Delta O_2 = \{([O_2]_{measured} - [O_2]_{saturation})/[O_2]_{saturation}\} \times 100$) is the primary driver of air-sea gas exchange (details in Section 4.1.1). Mixed layer depths were calculated from float-measured temperature, salinity, and pressure profiles according to de Boyer Montégut (2004) using a potential temperature threshold of 0.2°θ difference from the value at ten meters depth. Consideration of saturation anomaly is important, because shifts in supersaturation state, or the percent difference of oxygen concentration relative to full saturation, reflect seasonal changes in temperature, biological production, and mixing.

Table 1
Float names, deployment information, and number of profiles in each study region for SOS-Argo floats.

Float name	UW float #[a]	WMO #[a]	Date deployed	Deployment position	Number of profiles in KE regions[b]:		
					North	Central	South
KE-8	8381	5904028	Mar-04 2013	40.5°N, 149.7°E	33	0	0
KE-7	7665	5904033	Mar-04 2013	39.3°N, 149.3°E	192	35	0
KE-6	8382	5904025	Mar-03 2013	38.2°N, 149.0°E	110	135	0
KE-5	8394	5904031	Mar-01 2013	34.7°N, 147.9°E	29	171	0
KE-4	8387	5904027	Feb-28 2013	33.5°N, 147.5°E	68	77	0
KE-3	8375	5904030	Feb-28 2013	32.3°N, 147.1°E	81	72	0
KE-2	8372	5904026	Feb-28 2013	31.2°N, 146.8°E	74	149	0
KE-1	5328	5904029	Feb-27 2013	30.0°N, 146.4°E	0	22	230
Total:					587	661	230

[a] UW float # and WMO # are used to find data through the UW and the international Argo program.
[b] Kuroshio Extension regions are defined in Section 3.1. For each float, the number of profiles sorted into each KE region is listed. For example, Float KE-5 primarily contributed data to the Central KE region (171 profiles), but also 29 profiles to the North KE region.

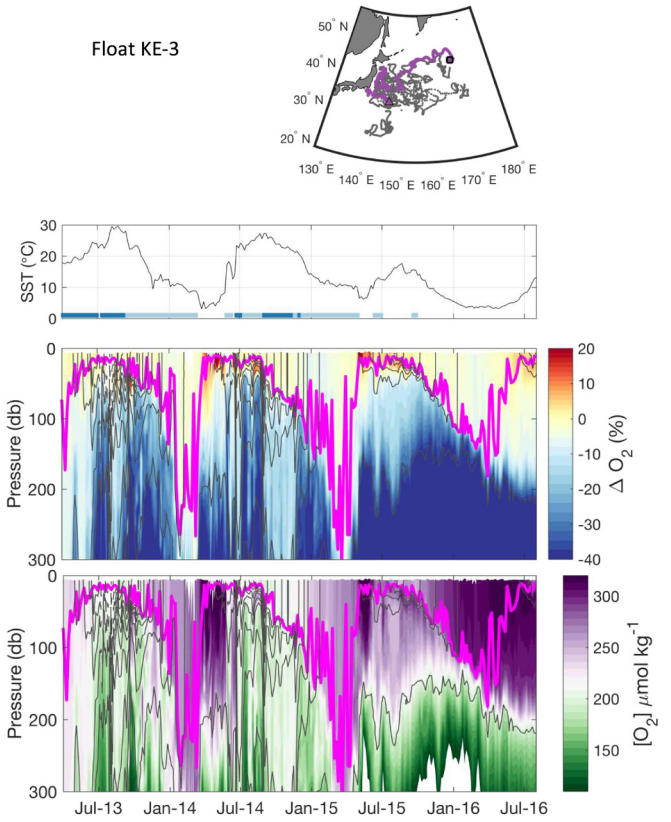

Fig. 2. Float KE-3 track, sea surface temperature (SST, ~ 5–6 m), oxygen saturation anomaly, ΔO_2, and oxygen concentration. Plotted underneath the SST curves are colors that correspond to the region (if any) into which profile was placed (North KE, light blue; Central KE, dark blue; and South KE, green (not observed for this float); regional definitions in Section 3.1 and Fig. 3). The mixed layer depth is plotted in magenta (de Boyer Montégut et al., 2004). The oxygen concentration in the upper ocean follows a seasonal pattern, with a summertime decrease in $[O_2]$ that partially tracks changes in solubility. Below the mixed layer, $[O_2]$ initially increases in the spring and early summer followed by fall and winter decreases. Mixed layer depth and isopycnals (light gray lines) fluctuate significantly in the first two years. Very large ΔO_2 and $[O_2]$ are measured for profiles when KE-3 neared the coast of Japan. (For interpretation of the references to colour in this figure legend, the reader is referred to the web version of this article).

Fig. 2 illustrates the multiple biogeochemical regions sampled by an individual float over a three-year time period in this region (equivalent plots for floats KE-1-2, 4-8 in Fig. A.1). Sharp changes in isopycnal depths, MLD, and oxygen concentration or supersaturation reflect movement of an individual float from one biogeographical regime to another.

3.1. Separation of float measurements into biogeographical provinces

A mass balance interpretation of an individual float would result in a large apparent advective flux each time the float crossed into a different biogeochemical region. While a perfectly Lagrangian drifter would follow a specific water parcel, shear in the horizontal transport between the 1000 m park depth and the surface results in these floats frequently sampling a variety of surface waters. To avoid interpretation of data from individual floats which are sometimes transported to very different regions of the KE the remaining analysis will use regional groupings of float profiles with a box model to assess the upper ocean oxygen balance. While information about the spatial heterogeneity of ANCP within each region is lost, interpretation of averages over large spatial regions reduces the possibility of spurious signals from individual floats crossing between water masses.

Float profiles were grouped based on temperature and salinity (TS) as well as latitude and longitude. Assigning float profiles to different regions (Fig. 3A) based purely on geographic location would ignore seasonal movement of surface waters, while separation based on temperature and salinity (Fig. 3B) allows the measurements to be grouped into regions of similar seasonal cycles of oxygen supersaturation and mixed layer depth.

The North KE region (light blue) and Central KE region (dark blue) were separated in TS space along line 2 in Fig. 3B, which corresponds to the boundary between the main Kuroshio Extension current and the transition zone where WSG waters from the north mix with Kuroshio Current and Extension waters from the south. This boundary moves north and south seasonally, which causes overlap of the profile locations in Fig. 3A. The subtropical gyre waters of the South KE region were separated from the Central KE region in TS space along line 1. Profiles in coastal waters with very high oxygen supersaturation (20–60%) and true WSG waters were removed from the North KE region by filtering out measurements colder and fresher than line 3. The divisions in TS space were empirically determined to create three regions with distinct seasonal cycles of supersaturation and mixed layer depth (Fig. 4). Boundaries were tested by shifting the slope and intercept of boundary lines in TS space to minimize the spread in these two parameters for each region and to group similar profiles. Three boxes were the minimum needed to create relatively uniform seasonal patterns; addition of more boxes was not possible without creating boxes with observational gaps. While TS criteria were the main determinant of separation into each region, float profiles over ~ 1.5 degrees latitude outside of the box boundaries indicated in Fig. 3A were removed from the analysis (dark gray points) to avoid extrapolation of fluxes to poorly represented areas.

Density was calculated from float temperature and salinity and smoothed using a 3-week running mean to reduce apparent oxygen changes in the mass balance estimates due to heaving. To combine float measurements into a regular, gridded time series, profiles were averaged on these smoothed isopycnals in two-week bins, chosen based on a typical residence time of oxygen in the surface ocean. For each two-week bin, oxygen measurements from individual profiles were interpolated to find the values at each isopycnal layer in the smoothed density grid. Measurements from all floats within a given region and two-week bin were then averaged at each layer. Daily parameter values were interpolated between two-week averages at each model box depth in order to calculate daily air-sea fluxes. Float deployment locations, identifying information, and contribution to each of the KE regions are described in Table 1. All floats except KE-8 contributed profiles to multiple KE regions; KE-8 only surfaced in the North KE region.

Overlaying surface supersaturations for each region into a single year illustrates the seasonal differences in oxygen (Fig. 4). Two-week mean supersaturations for each region are blue lines with ± 1 s.d. represented by blue shading. Individual points are colored by float to indicate the mix of floats that contribute to each region. Float profiles from the North KE measure the strongest supersaturations, with a peak in June of over 5% ΔO_2 that corresponds with the onset of the shallowest MLDs. The spring increase of ΔO_2 up to the peak in June has both the most rapid increase in supersaturation and the largest variance of any time period in any region. Surface waters in the North KE remain generally supersaturated until October, with the exception of a few floats that measure values at or near saturation. From November to the end of March this region is strongly undersaturated in oxygen, with a mean that varies from -3 to -5% ΔO_2 while mean MLDs range between 115 and 140 m.

The Central KE is only weakly supersaturated during the summer, with the mean ΔO_2 consistently between 0% and 2% and no obvious peak. Winter undersaturation in this region is strong, beginning in September, two months earlier than in the North KE, bottoming out at -3 to -4.5% in January before returning to positive supersaturation at the beginning of March. Mean MLDs in the Central KE region average

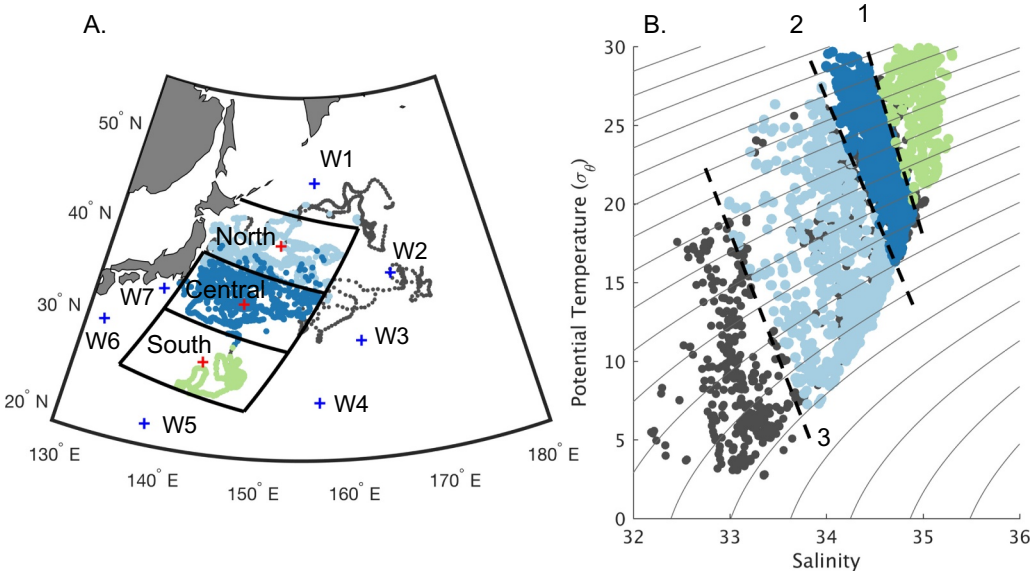

Fig. 3. (A) Kuroshio Extension area divided into three biogeochemical regions based on geographic location and (B) temperature salinity relationships of the surface measurements. The three regions (North KE, light blue; Central KE, dark blue; and South KE, green) are primarily separated along the black dashed lines in the TS plot (B). The North KE and Central KE regions were divided along line 2 in the TS plot. This partitions the surface measurements following the north and south seasonal movement of the KE. Colder, fresher coastal measurements with higher oxygen supersaturations that are more similar to the Western Subarctic Gyre were removed from the North KE region along line 3. The Central KE and South KE regions were separated along line 1. Data from locations greater than ~1.5 degrees latitude outside of the boxes in (A) were not used. Oxygen concentration differences used to calculate advection fluxes were determined from World Ocean Atlas data at the locations labeled W1-W7 (blue +'s) and data at the region centers (red +'s). Regional boundaries (clockwise from the upper left hand corner) are: North, 44°N × 146°E, 41°N × 163°E, 34.5°N × 158°E, 38°N × 142°E; Central, 38°N × 142°E, 34.5°N × 158°E, 28.5°N × 153.5°E, 31.5°N × 138.5°E; South, 31.5°N × 138.5°E, 28.5°N × 153.5°E, 22.5°N × 149°E, 25°N × 135°E. (For interpretation of the references to colour in this figure legend, the reader is referred to the web version of this article).

~ 15 m in the summer and ~ 200 m in the winter.

The South KE region has a smaller seasonal amplitude in supersaturation throughout the year than either of the more northern regions. The summertime is consistently above saturation at 1–3% with a peak in July, but with significantly lower supersaturation than the North KE. Wintertime waters are mainly near saturation from November through March with a low in January and February of -1 to -2% ΔO_2, when observed MLDs are at ~ 80 m. While it would be preferable to have a wide range of floats covering the entire South KE region, as in the Central and North KE regions, the mixed layer supersaturation and MLD seasonal cycles from KE-1 were distinct from the two northern regions and repeated over the three years. That, coupled with the lower short-term variance observed in the subtropical waters supported inclusion of the South KE region using the observations from a single float. The increased uncertainty in the South KE relative to the regions with multiple floats is discussed in Section 4.1.5 below.

Supersaturation time series with depth and mixed layers for each region are plotted in Fig. 5. The North KE region has a significant sub-mixed layer supersaturation in the summer. Maximum MLD is relatively constant at 135–150 m for all three years. Sub-mixed layer supersaturations decrease rapidly with depth. The Central KE region displays much less sub-mixed layer positive supersaturation in the summer and more variable mixed layers, with a deepest depth of ~ 189 m the first winter and 288 m the 2014–2015 winter. A break in data coverage occurs in the latter part of the 2015–2016 year as floats left the region to the north and east. In the South KE, large sub-mixed layer positive supersaturations are observed over a broader depth range than in the North KE. Mixed layers are shallower with maxima between 92 and 122 m.

4. Model description and discussion

4.1. Upper ocean mass balance

Float oxygen measurements were analyzed using a mass balance framework adapted from Bushinsky and Emerson (2015) in which physical fluxes influencing oxygen in the upper ocean are calculated, compared to the observed change in oxygen, and the residual is net biological oxygen production and any terms not considered in the mass balance plus all errors. This allows the use of oxygen as a tracer for biological carbon export from the upper ocean, a process that helps set the spatial pattern of air-sea carbon dioxide fluxes (Toggweiler and Sarmiento, 1985) and the size and extent of oxygen minimum zones (Hofmann and Schellnhuber, 2009). The model is quasi-one-dimensional, with each region represented by a variable height mixed-layer and a series of 10 m layers below this down to 400 m. Each term in the mass balance equation is explicitly calculated in depth space:

$$\frac{d(h[O_2])}{dt} = F_{A-S} + F_H + F_W + F_E + F_{\kappa z} + F_{Resid.} \quad \text{mol m}^{-2}\,\text{d}^{-1} \tag{1}$$

where h is the height of each upper ocean layer, $F_{A\text{-}S}$ is the exchange across the air water interface, F_H is horizontal advection, F_W is vertical advection, F_E is entrainment, $F_{\kappa z}$ is diapycnal diffusivity, and $F_{Resid.}$ is the residual oxygen term that typically represents biological production plus all errors and any uncounted physical term. Horizontal fluxes act at the boundary of each region, and the residual term ($F_{Resid.}$) is calculated each day with model concentrations reset to observations.

4.1.1. Air-sea gas exchange flux

The air-sea exchange of oxygen is comprised of two pathways, diffusive gas exchange and bubble processes, both of which are governed by the degree of oxygen supersaturation and wind speed. We chose a gas flux parameterization (Liang et al., 2013) that explicitly includes two types of bubbles, large and small, to accurately estimate the air-sea oxygen flux. Emerson and Bushinsky (2016) found that, of the gas flux parameterizations tested, Liang et al. (2013) was best able to reproduce both N_2 measurements at Ocean Station Papa (OSP) and noble gas ratios collected at multiple sites, which are independent tracers sensitive to the fraction of bubbles injected into the ocean during gas exchange. Subsequent work tuning the bubble contribution in the Liang et al. (2013) model to the total air-sea flux using N_2 observations at OSP (Yang et al., 2017) determined that reducing the small and large bubble flux components yields an improvement of the wintertime fit to the data, and this is the model we describe below. (See the Appendix to Emerson and Bushinsky, 2016, for greater detail of the model equations.) The total air-sea oxygen flux ($F_{A\text{-}S}$) is the sum of the air-sea interface exchange (F_S), small, completely collapsing bubbles (F_C), and large, partially collapsing bubbles (F_P):

$$F_{A-S} = F_S + F_C + F_P \quad \text{mol m}^{-2}\,\text{d}^{-1} \tag{2}$$

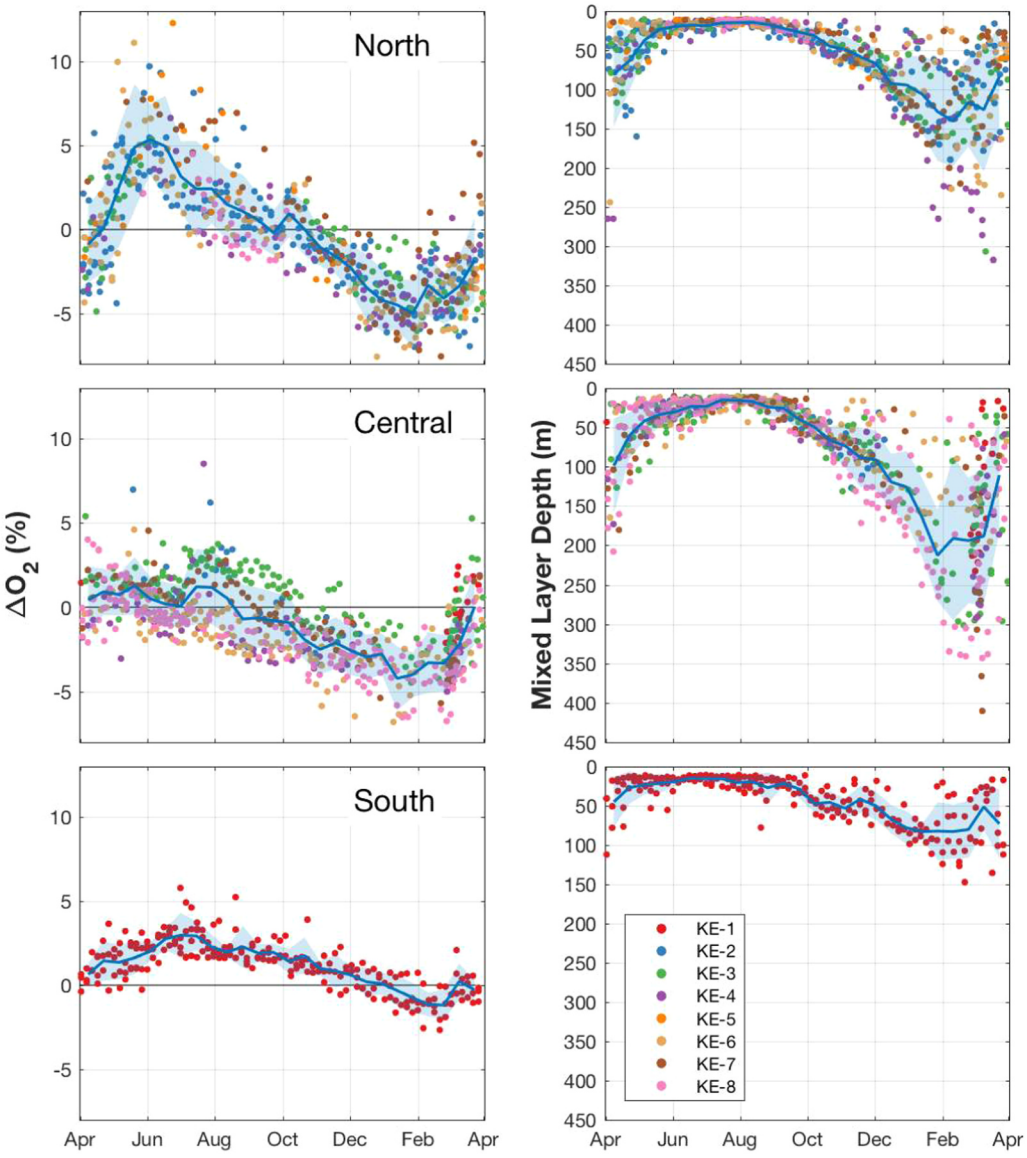

Fig. 4. Percent supersaturation (ΔO_2) and MLD for each region. Surface supersaturation and calculated MLD from all profiles and years are plotted against month to create a single composite year. Colored points represent a surface oxygen measurement, with different colors indicating different floats. Measurements are divided into separate regions by a combination of TS relationships and geographic location (See Section 3.1 and Fig. 3) in order to produce repeated seasonal cycles of supersaturation and MLD. Blue lines and shaded blue regions represent two-week means ± 1 standard deviation. (For interpretation of the references to colour in this figure legend, the reader is referred to the web version of this article).

F_S is a function of oxygen concentration ($[O_2]$, μmol kg^{-1}) difference from saturation ($[O_{2,sat}]$) times an air-sea interface mass transfer coefficient ($k_{S,O2}$):

$$F_S = k_{S,O2}\left([O_{2,sat}] - [O_2]\right)\frac{\rho_w}{10^6} \text{ mol m}^{-2}\text{ d}^{-1} \quad (3)$$

where ρ_w is seawater density (kg m^{-3}). Liang et al. (2013) uses the NOAA-COAREG linear relationship between k_S and the air-side friction velocity (U_a^*) to evaluate the wind speed ($U_{10,}$ m s^{-1}) and Schmidt number (S_{O2}) dependent mass transfer coefficient:

$$k_{S,O2} = 1.3 \times 10^{-4} U_a^* \left(\frac{S_{O2}}{660}\right)^{-0.5} \text{ m s}^{-1} \quad (4)$$

where

$$U_a^* = C_d^{0.5} U_{10} \text{ m s}^{-1} \quad (5)$$

and 660 is the Schmidt number for CO_2 in seawater at 20 °C. The air-side friction velocity, U_a^*, is the product of a dimensionless drag coefficient and wind speed ($C_d = 0.0012$ below 11 m s^{-1}, $(0.49 + 0.065 \times U_{10}) \times 10^{-3}$ between 11 and 20 m s^{-1}, and 0.0018 above 20 m s^{-1}). Note that a positive flux means that oxygen is going into the ocean and a negative flux represents gas lost to the atmosphere.

Temperature measurements from profiling floats reflect the temperature of the bulk mixed layer, however heat loss at the air-sea interface can lower the skin layer boundary temperature by a few tenths of a degree (Hasse, 1971). This can impact air-sea exchange, as gas exchange happens directly at the interface, where the saturation concentration that drives the air-sea exchange is impacted by the skin temperature.

The impact of the cool skin effect is reflected in changes to $[O_{2,sat}]$ and S_{O2}. A difference in temperature of 0.4–0.8 °C would result in a change of ~ 2% to both $[O_{2,sat}]$ and S_{O2}, but in opposite and off-setting directions, resulting in a negligible impact (Appendix B, Fig. B.1 and B.2). Therefore, the cool skin impact on diffusive exchange is not included in these air-sea flux calculations. Gas exchange can also be impacted by diurnal warming, however a cooler ocean skin temperature is far more common (Alappattu et al., 2017).

Small bubbles that completely collapse add gas to the water as a function of wind speed but are independent of saturation state:

$$F_C = 5.56\,\beta (U_w^*)^{3.86} X_{O2} \text{ mol m}^{-2}\text{ s}^{-1} \quad (6)$$

where X_{O2} is the mole fraction of oxygen in the atmosphere. β is the correction factor for the bubble mechanisms determined from comparison with N_2 data at OSP. Recent work indicates the value we

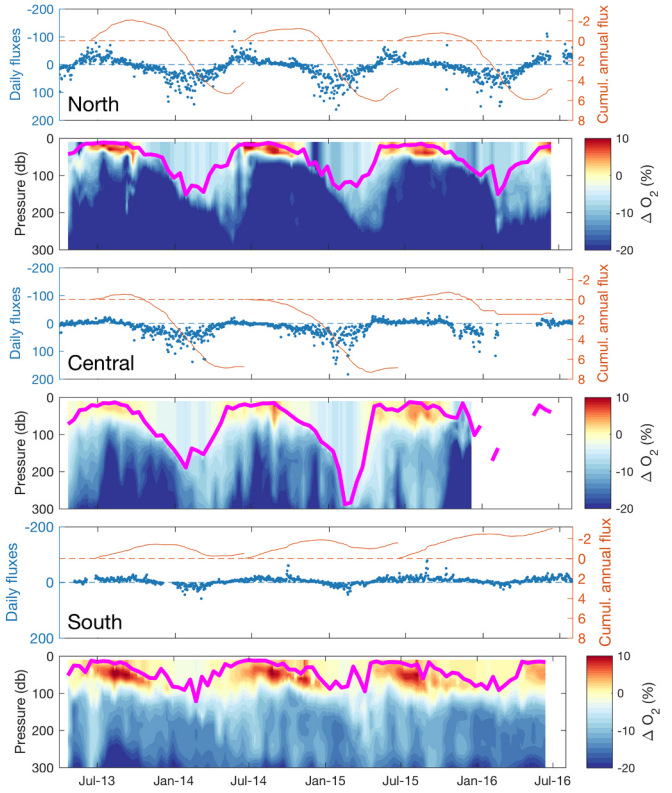

Fig. 5. Calculated daily air-sea gas fluxes (mmol O_2 m^{-2} d^{-1}), cumulative annual fluxes (mol O_2 m^{-2}), and vertical supersaturation (%) time series for KE regions. Positive fluxes are into the ocean, with axis direction reversed to illustrate the connection to the saturation state of the surface ocean. The North KE (top two panels) displays a strong summertime outgassing due to high surface supersaturations that is offset by a wintertime flux of oxygen into undersaturated waters. Very little surface supersaturation is present in the Central KE (middle two plots), yielding little summertime outgassing. Winter undersaturation and deep mixed layers cause a very strong influx of oxygen in the Central KE. The highest supersaturations in the South KE occur below the summer mixed layer, but overall supersaturation for much of the year results in a net out gassing of oxygen in all three years.

determined previously (β = 0.29; Yang et al., 2017) is close to the result obtained with a much larger dataset (S. Emerson, unpublished results). U_w^* is the water-side friction velocity calculated from U_a^* and the densities of air (ρ_a) and water (ρ_w):

$$U_w^* = \left(\frac{\rho_a}{\rho_w}\right)^{0.5} U_a^* \ \text{m s}^{-1} \tag{7}$$

Large bubbles that are pushed into the ocean and rise back to the surface without collapsing exchange gas according to the saturation state of the surrounding water:

$$F_P = 5.5\,\beta (U_w^*)^{2.76}\left(\frac{S_{O2}}{660}\right)^{-2/3}\left([1+\Delta_P][O_{2,sat}]\frac{\rho_w}{10^6} - [O_2]\frac{\rho_w}{10^6}\right) \ \text{mol m}^{-2}\,\text{s}^{-1} \tag{8}$$

Here, Δ_P is the fractional increase in pressure experienced by bubbles driven below the surface due to breaking waves at high wind speeds:

$$\Delta_P = 1.5244\ U_w^{*1.06} \tag{9}$$

For air-sea flux calculations, temperature, salinity, and surface oxygen concentration are determined from float measurements. Sea level pressure, used to calculate oxygen saturation state, is derived from NCEP reanalysis. Wind speed is calculated from Advanced Scatterometer (ASCAT) wind vectors (Bentamy et al., 2008). Air-sea fluxes were calculated on a daily time step from interpolated float measurements. This matches the wind speed temporal resolution used in the Liang et al. (2013) flux parameterization and avoids an averaging bias due to the non-linear relationship between wind speed and air-sea fluxes. Uncertainty in $F_{A\text{-}S}$ is assessed using a Monte Carlo approach described in Section 4.1.5.

In all regions, F_S is the most important term, but the relative contributions of F_S, F_C, and F_P to $F_{A\text{-}S}$ is a function of surface supersaturation and wind speed. In the North and Central regions, F_S is between half and two thirds of the total flux, with F_P between one quarter and one third and F_C the remainder (Appendix C). In these two regions, each flux is net positive to the ocean. In the South region, F_S is out of the ocean and larger in magnitude than the total outgassing, which is reduced through much smaller contributions of both bubble terms.

Emerson et al. (2008) identified uncertainty in the oxygen measurement as contributing ~ 50% error to estimates of net oxygen production because of its influence on the air sea flux. By directly measuring the difference between the partial pressure of oxygen in the air and water, the SOS-Argo float measurements result in a great improvement in the accuracy of the air-sea oxygen flux calculation. A comparison of the impact of this increased accuracy in reducing uncertainty in the air-sea flux term is described in Section 4.1.5. Uncertainty in the NCEP atmospheric pressure estimate does not contribute to error in the air-sea flux calculation because the same pressure measurement is used for both air and pO_2 determinations.

4.1.2. Entrainment

Entrainment at each time step was calculated from observed changes in the mixed layer depth using a 0.2°θ threshold as described in de Boyer Montégut et al. (2004). The entrainment flux is:

$$F_E = [C]\rho_w \frac{dh_E}{dt} \ \text{mol m}^{-2}\,\text{d}^{-1} \tag{10}$$

where *[C]* (μmol kg^{-1}) is the concentration of water being entrained or left behind (in shoaling mixed layers) and dh_E/dt (m/d) is the height of the mixed layer change for a model time step. Entrainment was calculated at the start of each time step, with the re-distributed height of the top, mixed layer box, and the box below determining the movement of moles of oxygen before subsequent fluxes were calculated using the new gradients.

4.1.3. Advection

The horizontal advection flux was determined from both geostrophic advection taken from AVISO altimetry-derived daily geostrophic current velocities (http://www.aviso.altimetry.fr) and Ekman transport calculated from ASCAT daily wind component vectors (Bentamy et al., 2008). Geostrophic and Ekman velocity vectors are calculated along box boundaries at 0.5° intervals and projected onto the box boundaries to determine the orthogonal component. Daily average surface velocities were calculated for each boundary (north, south, east, and west) and 3-month averages were calculated from the daily values. Mass must be conserved to avoid spurious advective oxygen fluxes. Monthly averages are adjusted to set net flow to zero over each 3-month period while retaining proportional differences between flow across each boundary. The net horizontal advective flux across each regional box boundary ($F_{H:\ N,S,E,W}$) was calculated as:

$$F_{H:N,S,E,W} = \frac{\{[C]_{Geo}\rho V_{Geo} h_{ML} + [C]_{Ekman}\rho V_{Ekman}\}}{A} \ \text{mol m}^{-2}\,\text{d}^{-1} \tag{11}$$

where $[C]_{Geo}$ and $[C]_{Ekman}$ (μmol kg^{-1}) are the source concentrations for the direction of flow (in or out of the box), V_{Geo} (m^2 d^{-1}) is the mean daily geostrophic velocity times the box edge length, h_{ML} (m) is the mixed layer depth, V_{Ekman} is the daily mean Ekman transport times the box edge length (m^3 d^{-1}), and A (m^2) is the box area. Total horizontal advective flux is:

$$F_H = F_N + F_S + F_E + F_W \text{ mol m}^{-2}\text{ d}^{-1} \quad (12)$$

where sign convention is positive represents flow into a given region. Advection of oxygen is achieved by determining the oxygen concentration of the water entering or leaving each box for exchange between the three KE regions or the World Ocean Atlas (WOA) concentration differences between the box center and the appropriate exterior point (W1-W7, Fig. 3). Because we rely on WOA concentration gradients for exterior boundaries, the advective flux we calculate is not entirely independent for each year. It is also important to note that we include no horizontal transport between the bottom of the mixed layer and our 400 m model boundary due to a lack of flow information at depth.

Vertical advection (F_W) due to Ekman pumping is calculated at the resolution of the ASCAT wind product (Bentamy et al., 2008, 0.5° grid size) and averaged over the area of each region. Ekman velocities (Hartmann, 1994) from the wind stress curl multiplied the float-measured average regional concentration gradient give the vertical advection fluxes. For the purposes of this model, F_E represents the redistribution of oxygen between model boxes that occurred due to vertical processes from the prior time step while F_W is the magnitude of the vertical flux due to Ekman pumping, part of which influences MLD changes for the next time step.

4.1.4. Vertical eddy diffusion

Diapycnal diffusivity is calculated at each time step according the diapycnal diffusivity coefficient and the oxygen concentration gradient:

$$F_{\kappa z} = \frac{d[O_2]\frac{\rho_w}{10^6}}{dz}\kappa \text{ mol m}^{-2}\text{ d}^{-1} \quad (13)$$

where κ (m^2 s^{-1}) seasonally varies at the base of the mixed layer according to a surface heat flux determined diffusivity at the Kuroshio Extension Observatory (Cronin et al., 2015). κ at the base of the mixed layer follows a sine function with a maximum of $1 \times 10^{-2.3}$ m^2 s^{-1} in the winter (March) and a minimum of $1 \times 10^{-3.7}$ m^2 s^{-1} in the summer (August) and decays to a background value of 5×10^{-5} m^2 s^{-1} (Whalen et al., 2012) over 20 m (Bushinsky and Emerson, 2015; Sun et al., 2013).

4.1.5. Monte Carlo error estimate

Uncertainty in fluxes was calculated using a 1000 iteration Monte Carlo simulation. Uncertainties for each air-calibrated oxygen sensor were taken from Bushinsky et al. (2016) and range from ± 0.18–0.34%. Uncertainties in oxygen concentration are propagated through advection between regional boxes at each time step. Following Bushinsky and Emerson (2015), a ± 15% uncertainty was assigned to each air-sea flux term (F_S, F_C, F_p), which gives an approximate ± 26% uncertainty for the total air-sea flux. Additional uncertainties of ± 50% were added to horizontal Ekman advection velocities, geostrophic advection velocities, vertical advection velocities, mixed layer diffusivity, and the background diffusivity.

Uncertainty in the oxygen measurements has the largest impact on the air-sea flux calculation. To test the reduction in uncertainty afforded by the air calibration of oxygen optodes used in this study, we ran two additional 100 iteration Monte Carlo simulations: one with the above sensor uncertainties and one with optode sensor uncertainty set at ± 2%, uncorrelated between optodes (Appendix C). The example uncertainty of ± 2% is approximately the uncertainty of reanalyzed Argo oxygen (Takeshita et al., 2013). The standard deviation of the cumulative air-sea flux over the first year of this study increases by ~ 3 times for the North and Central regions and ~ 9 times for the South region. The largest increase in uncertainty is in F_S, followed by F_P. F_C is unaffected by uncertainty in the optode measurement because the effect of collapsing bubbles is independent of the surface concentration.

In addition to highlighting the importance of highly accurate oxygen measurements, this also illustrates the benefit of averaging multiple oxygen sensors in one region. The North and Central regions each include observations from seven floats, while the South region only contains one float. As a result, uncertainty in the air-sea flux in the South region is both much larger as a fraction of the total flux and much more sensitive to uncertainty in the oxygen measurement, despite the greater air-sea concentration gradients observed in the North and Central regions and higher average wind speeds. This assumes that errors are uncorrelated between floats. This is likely a valid assumption, as the air calibration is primarily a measurement of the difference in partial pressure between the ocean and atmosphere and relatively independent of the atmospheric pressure. Uncertainties in the water vapor pressure or the mole fraction of oxygen in the atmosphere are small. This leaves differences in how well characterized the optode response is as a function of temperature and oxygen partial pressure, which should be uncorrelated, as these optodes are individually calibrated.

4.2. Fluxes determined from oxygen mass balance

To understand the physical fluxes of oxygen in order to isolate the biological component and its relative magnitude in this region, we apply the box model described in Section 4.1 to each region over the three annual cycles of data. Annual cycles were chosen based on the seasonal cycle of mixed layer depth with a start of June 15 best matching the summer shoaling in all three regions. The North and South regions were analyzed for 2013–2016, while in the Central KE only 2013–2014 and 2014–2015 were considered due to a data gap in year 3 from floats leaving the Central KE region. Cumulative flux and residual oxygen terms are plotted in Fig. 6 and compiled in Table 2. Annual fluxes are the sum total of summertime outgassing and wintertime influx to the ocean. The summertime flux to the atmosphere is driven by both biological production and the warming of the shallow mixed layer, which reduces the solubility and increases ΔO_2. A portion of the organic carbon produced is transported from the mixed layer in the form of particulate organic carbon or dissolved organic carbon. Of this, some fraction is respired below the summertime mixed layer but above the depth of winter ventilation. We are interested in the net

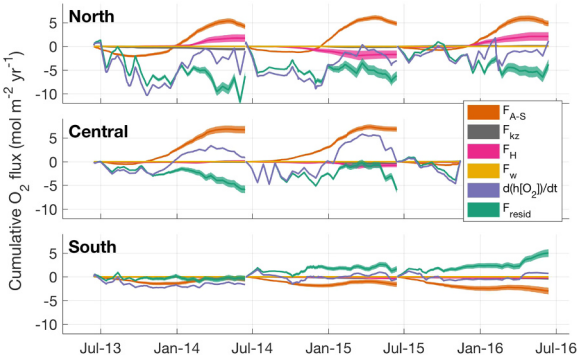

Fig. 6. Mean cumulative oxygen fluxes calculated from the box model for Kuroshio Extension regions. An increase in the lines indicates a flux of oxygen into the water column, a decrease represents a loss. The oxygen flux calculated from measurements ($d\{h[O_2]\}/dt$, Eq. (1), purple line/area) minus the calculated physical fluxes: air-sea exchange ($F_{A\text{-}S}$, orange), horizontal advection (F_H, magenta), vertical advection (F_W, yellow), and diapycnal diffusion ($F_{\kappa z}$, gray) equals the residual term (dark green). F_E equals zero once model boxes are integrated vertically down below the depth of the mixed layer and is therefore omitted. The residual term represents net community production, any unaccounted for physical terms, and all errors. The Central KE mass balance is stopped midway through year 3 due to a data gap. Fluxes are integrated to the depth of each winter mixed layer, which vary for the different years and regions. (For interpretation of the references to colour in this figure legend, the reader is referred to the web version of this article).

Table 2
Summary of oxygen fluxes for each region (mol O_2 m^{-2} yr^{-1})[a].

	North mean (n = 3)[g]	MC uncertainty[h]	Central mean (n = 2)[g]	MC uncertainty[h]	South mean (n = 3)[g]	MC uncertainty[h]
$F_{A\text{-}S}$[b]	4.6 ± 0.3	0.5	6.8 ± 0.1	0.7	− 1.7 ± 1	0.6
F_H[c]	0.7 ± 1.7	0.8	− 0.3 ± 0.5	0.2	− 0.3 ± 0	0.2
F_{kz}[d]	− 0.2 ± 0.3	0.1	− 0.2 ± 0.1	0.1	− 0.3 ± 0.1	0.1
$F_{Resid.}$[e]	− 5.4 ± 1.1	1.0	− 5.9 ± 0.1	0.7	2.1 ± 2.2	0.7
$d\{h[O_2]\}/dt$[f]	− 0.9 ± 1.7	0.1	0.4 ± 0.5	0.1	− 0.5 ± 1	0.0

[a] Fluxes are described in Section 4.1, Eq. (1). F_E equals zero once model boxes are integrated vertically down below the depth of the mixed layer. F_W is an order of magnitude smaller than the other fluxes and omitted from this table.
[b] $F_{A\text{-}S}$ is the total exchange across the air water interface.
[c] F_H is horizontal advection.
[d] F_{kz} is diapycnal diffusion.
[e] $F_{Resid.}$ is the residual oxygen term to balance Eq. (1).
[f] $d\{h[O_2]\}/dt$ is the time rate of change of oxygen in the upper ocean.
[g] Mean values for the three years ± 1 s.d. of the annual means are listed, representing interannual variability during the study years.
[h] Monte Carlo uncertainty for each region, representing the uncertainty estimate for a given year (n = 1000). Summary of fluxes plotted in Fig. 6.

transfer of oxygen and carbon between the atmosphere and the ocean over the annual cycle and therefore integrate down to the depth of the wintertime mixed layer. This results in a lower net community production estimate than if only the summertime mixed layer is evaluated but is a better representation of the total flux from the atmosphere to the ocean on time scales of greater than one year. Significant interannual variability in mixed layer depths was observed in the Central and South KE regions. Wintertime mixed layer depths used for integration of each region are North: 170, 150, and 155 m, Central: 200 and 300, and South: 140, 110, and 110 m, for 2013–2014, 2014–2015, and 2015–2016, respectively.

The dominant calculated term in each region is the air-sea flux. Water saturation state and wind speed drive air-sea exchange, with summertime supersaturation due to warming and biology causing an efflux of oxygen and wintertime undersaturation from cooling, mixing, and biological processes driving an influx of oxygen during a typical annual cycle. Upper ocean supersaturation state is plotted with daily air-sea fluxes (mmol m^{-2} d^{-1}) on the left y-axis (blue points) and cumulative annual fluxes (mol m^{-2} yr^{-1}) on the right y-axis (red lines) in Fig. 5.

The large amplitude seasonal cycle in the supersaturation state of the North KE region drives an outgassing of -2.1, -1.2, and −0.8 mol of O_2 m^{-2} (positive fluxes are to the ocean) during the summer that is outweighed by a much stronger influx of oxygen to the ocean in the winter, resulting in a mean annual $F_{A\text{-}S}$ of 4.6 ± 0.3 mol O_2 m^{-2} yr^{-1} into the ocean (Fig. 6, Table 2). Two uncertainties are presented for each flux in Table 2: the standard deviation of the annual means (n = 2 or 3), which represents interannual variability during the study and the Monte Carlo uncertainty, which represents uncertainty in the estimate for each individual year.

Seasonal cycles are fairly repeatable for the three years of North KE data, with a smaller annual air-sea flux in the first year and the largest annual flux in the second year (Fig. 6). In the first two summers, the integrated loss of oxygen calculated from measurements ($d\{h[O_2]\}/dt$) is greater than the air-sea flux, indicating that oxygen production due to surface biological production is balanced by respiration deeper in the water column or that the observed positive supersaturation and outgassing is due to temperature driven changes in solubility. Net respiration could also be responsible for the calculated annual loss of oxygen but would require an imported source of organic carbon. An imported source of carbon would have to be in the form of semi-labile DOC that was produced outside of the region but not consumed and was brought in through advection, then respired. The magnitude of the seasonal cycle of semi-labile DOC throughout the ocean is 5–30 μM (Hansell and Carlson, 2001). At the highest end of this range, 30 μM DOC respired in a mean mixed layer depth of 75 m would consume ~3 mol O_2 m^{-2}, which would be a significant fraction of the oxygen deficit. However, a problem with this explanation is that the Kuroshio waters that feed our study area are depleted of DOC (Hansell and Carlson, 2002). The third summer has a moderate summertime inferred production, with a maximum residual flux of 1.0 mol O_2 m^{-2}. In the winter, a strong influx of oxygen driven by undersaturated waters and high wind speeds is reflected in an increase in the measured oxygen change.

Advection is a significant contributor to the total North KE flux, with an addition of 1.9 and 2.2 mol O_2 m^{-2} in the first and third years and a removal of −1.9 mol O_2 m^{-2} in the second year. The change in sign here likely reflects interannual variations in the mean current direction due to changes in the location of the Kuroshio Extension jet. During 2013 and 2014 the KE was in its more stable state, with coherent transport that diverges from the coast of Japan further north than when in an unstable mode (Oka et al., 2015). In 2015 the mean KE position began moving South to ~35°N, where it remained in 2016, though with significant sub-annual variability (Qiu et al., 2017). Diapycnal diffusion is a relatively minor flux, removing −0.6 mol O_2 m^{-2} in the first year, −0.2 mol O_2 m^{-2} in the second and is indistinguishable from zero in the final year. The total mean residual oxygen flux for the North KE region is a loss of -5.4 ± 1.1 mol O_2 m^{-2} yr^{-1}. This is $F_{Resid.}$, the sum of the net annual biological flux and any physical terms or errors unaccounted for in Eq. (1). For all regions, the distribution of $F_{Resid.}$ from the Monte Carlo error estimate was close to normal. In prior work (Bushinsky and Emerson, 2015; Yang et al., 2017), net biological production is inferred from this residual flux. However, a multi-year respiration of oxygen of this magnitude over a large area is unrealistic. Furthermore, horizontal transport is not estimated below the mixed layer geostrophic advection and Ekman flow. We will discuss the implications of this and a possible physical explanation below.

In the Central KE, weak summertime supersaturation yields very little outgassing to the atmosphere and is entirely dominated by strong wintertime undersaturation that drives an average flux of ~60 mmol O_2 m^{-2} d^{-1} into the ocean during the winter. The resulting net $F_{A\text{-}S}$ is 6.7 ± 0.8 and 6.8 ± 0.5 mol O_2 m^{-2} yr^{-1} for 2013–2014 and 2014–2015, respectively. The accounted for advection and diffusion are minor fluxes relative to the air-sea exchange. The observed flux of oxygen follows a similar pattern to the North KE of loss in the summer and gain in the winter, with the difference between the input from the atmosphere and the observed changes indicating a net oxygen loss ($F_{Resid.}$) of -5.9 ± 0.1 mol O_2 m^{-2} yr^{-1}.

The South KE region is distinctly different than the North or Central KE regions. Summertime outgassing outweighs the wintertime influx of oxygen in all three years, with a maximum cumulative summertime air-sea flux of -1.4, -1.9, and -2.4 mol O_2 m^{-2} over the three years. In the first year, this summertime loss roughly follows the observed oxygen flux, indicating little to no annual residual flux (-0.3 ± 0.6 mol O_2 m^{-2}

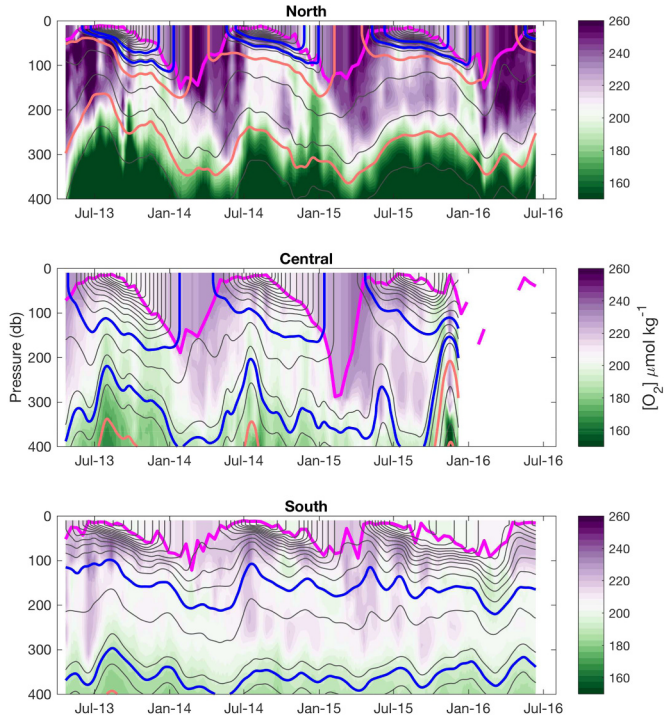

Fig. 7. Averaged oxygen concentrations as a function of depth and time for each region. Mixed layer depths are plotted in magenta and isopycnals (σ_θ) are thin gray lines (0.25 σ_θ spacing). Thick blue lines are the isopycnal bounds of Subtropical Mode Water (STMW, 25–25.6 σ_θ) and thick orange lines are Central Mode Water (CMW, 26–26.6 σ_θ). Interior CMW and STMW are seasonally ventilated in the northern box, but waters with the density of STMW do not connect with the ocean interior. Only STMW is ventilated in the Central box. Both water masses are present subsurface in the South box, but the mixed layers are never deep enough to entrain and expose either watermass to the atmosphere. (For interpretation of the references to colour in this figure legend, the reader is referred to the web version of this article).

yr^{-1}). In years two and three the outgassing to the atmosphere exceeds the observed oxygen flux, which results in a residual oxygen production of 1.7 ± 0.6 and 5.0 ± 0.8 mol O_2 m^{-2} yr^{-1}, or a three-year mean of 2.1 ± 2.2 mol O_2 m^{-2} yr^{-1}. While all regions display some sub-mixed layer oxygen supersaturation during the summer months, this signal is most pronounced in the South KE region (Fig. 5). Oxygen concentrations in the South KE region during the summer do increase slightly (Fig. 7), indicating some photosynthetic production below the summertime mixed layer. In contrast, oxygen concentrations below the shallow summer mixed layers in the North and Central KE regions do not display significant increases, indicating that the increase in supersaturation is due to warming of sub-mixed layer waters.

4.3. Oxygen uptake by mode water ventilation

The North and Central KE regions display little to no indication of a significant contribution of annual net community production to the annual oxygen flux. This is not to say that there is no organic matter production in these regions, but that when considered over an annual cycle to the wintertime mixed layer depth, the contribution of ANCP over these large areas is apparently overwhelmed by other physical fluxes. This is consistent with the low ANCP found in Palevsky et al. (2016) when integrated to the base of the wintertime mixed layer depth despite high summertime productivity. Instead, large annual oxygen deficits are present in both regions, indicating a physical removal of oxygen that is not present in our model. The most probable explanation is present in the subduction of mode waters. The KE region is the site of significant mode water formation (Suga et al., 2008, 2004), with subtropical mode water (STMW) formed in the Central KE region and central mode water (CMW) formed in the North KE regions. Mode water is formed from the subduction of mixed layer waters during the late winter through a combination of vertical flow across the base of the mixed layer and lateral induction of mixed layer waters due to spatial variations in the depth of the mixed layer (Suga et al., 2008).

Lateral advection of water along isopycnals below the mixed layer and lateral induction from sloped mixed layers are not represented in our model and could represent a significant unaccounted-for oxygen loss term. Time-series sections of oxygen concentration as a function of depth (Fig. 7) with overlaid isopycnals indicate the range of densities of the mode waters. The CMW (26–26.6 σ_θ, orange lines) is ventilated each year in the North KE region but is below the deepest mixed layer depths in the Central and South KE regions. Water with the densities of STMW (25 – 25.6 σ_θ, blue lines) is created and lost seasonally in the North KE region and is ventilated during the winter in the Central KE region. STMW is lighter than CMW, but still below the deepest mixed layers in the South KE region. From these figures, we can assume that mode water ventilation is an important part of the upper ocean gas budget in the North and Central KE regions, but not in the South region.

The concentration difference between mode waters prior to winter mixing and post ventilation represents the amount of oxygen taken up by a given parcel of water. If we assume that the residual oxygen flux calculated for the North and Central KE regions represents the amount of oxygen removed from the system by the mode water ventilation that is unaccounted for in our model, we can calculate the volume of mode water formed.

This calculation yields 4.0 ± 0.9 Sv of CMW formed in the North KE region and 7.6 ± 0.1 Sv of STMW formed in the Central (MW vol. = $\{F_{Resid.} \times \text{Area}\}/\{[O_2]_{\text{Final}} - [O_2]_{\text{Initial}}\}$). Suga et al. (2008) calculate subduction rates for binned density classes in the North Pacific, separating vertical transport at the base of the mixed layer, which is included in our model, and lateral induction. If we sum Suga's lateral induction values along the isopycnal ranges for CMW and STMW we determine rates of ~ 4.4 and ~ 6.1 Sv, respectively (Suga et al., 2008, Fig. 5b). In the North, our estimate of missing lateral transport agrees within the uncertainty with the Suga et al. (2008) calculation, while our estimate in the Central region is 25% greater.

A major assumption in this calculation is that the residual oxygen flux applies equally across each regional box and that mode water is being formed uniformly across an equal area. Additionally, there is significant interannual variability present in the formation and volume of these mode waters (Oka et al., 2015), so there may be differences due to variability. Suga et al. (2008) also calculate mode water subduction across the entire North Pacific, however the majority of the contribution due to lateral induction occurs over a similar geographic area as our study. Despite these assumptions, this mechanism presents a likely loss term similar in magnitude to the residual oxygen terms in each region. The wintertime formation of mode water through the Central and North regions is not captured in the simple horizontal transport term we include in the box model. With a vertically-resolved horizontal advection term that also accounted for induction due to spatial variations in mixed layer depth it would be possible to directly estimate the contribution of mode water ventilation to the upper ocean oxygen mass balance.

This calculation also assumes that no annual net community production is contributing to the air-sea oxygen fluxes in the North and Central regions, a conclusion we will discuss in the next section. If there

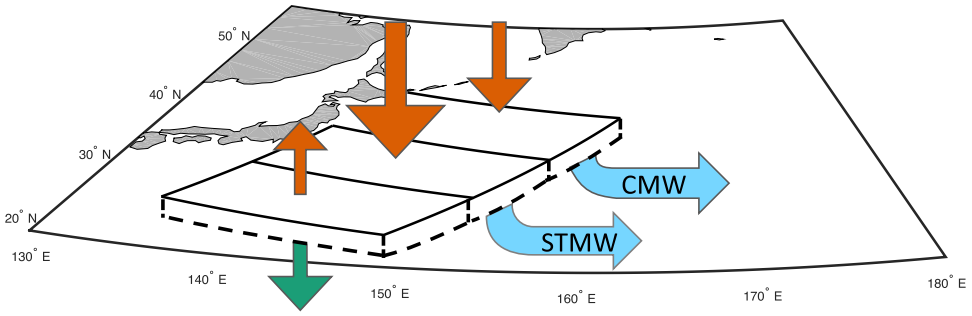

Fig. 8. Schematic of importance fluxes in the Kuroshio Extension regions. In the North and Central KE regions the oxygen mass budget is a balance of air-sea flux ($F_{A\text{-}S}$, brown arrows) and mode water formation (light blue arrows), with Central Mode Water (CMW) formed in the North and Subtropical Mode Water (STMW) in the Central KE region. In the South KE region, the air-sea exchange is due to a biological flux (F_J, green arrow). (For interpretation of the references to colour in this figure legend, the reader is referred to the web version of this article).

is a significant contribution of ANCP to the annual oxygen budget in these regions, it will increase the calculated mode water formation in direct proportion to the increase in the residual oxygen term. For example, if there is 1 mol O_2 m^{-2} produced in the North region, the amount of oxygen removed by mode water ventilation would need to be larger, and the amount of mode water laterally inducting into the interior would increase by ~ 1 Sv.

4.4. Contribution of annual net community production to air-sea fluxes

From these calculations and the box model results, we determine that the net annual oxygen balance of the Kuroshio Extension region is dominated by physical forcing in the Central and North regions, with biological production only a significant term in the South region (Fig. 8). We find little evidence for a biological driver of the significant carbon uptake in the North and Central regions of the Western North Pacific. Instead, as the Kuroshio waters move northward along the western boundary of the Pacific, the waters cool and are subducted into interior mode waters, carrying large amounts of oxygen and carbon.

Previous studies of net community production in the Western North Pacific have primarily been performed at times series stations off the coast of Japan. Of these, S1 (30°N, 145°E) is just within the northern border of the South KE box, the Kuroshio Extension Observatory (KEO, 32.4°N, 144.6°E) is within the Central box, K3 (39°N, 160°E) is in the North box and KNOT (44°N, 155°E) is just outside of the North box (Appendix D). Two sites of significant prior work, K1 (51°N, 165) °E and K2 (47°N, 160°E) are further north in the subpolar gyre and outside of our study area. One difficulty with comparisons to prior work is that many studies measured net biological production only during the productive months (Yasunaka et al., 2013) or had measurements only from the mixed layer (Fassbender et al., 2017). Yasunaka et al. (2013) estimated surface DIC changes using a neural network approach and calculated NCP after removing estimated air-sea fluxes, finding the highest summertime (March to July) NCP in a region that is similar to our North KE region.

Fassbender et al. (2017) estimate significant ANCP at KEO, within our Central KE region (Fig. D.1), with the strongest NCP from March to August. The Fassbender et al. (2017) study shares some of the differences from the current study as Yasunaka et al. (2013), in that the changes in DIC are from the mixed layer only. To add to the difficulty in comparison, our Central box encompasses a much wider region than the single point at KEO, representing a tradeoff between high sampling resolution and spatial coverage. It is likely that high ANCP is found at specific locations within these regions, but when averaged over the larger areas that represent the North Pacific carbon dioxide uptake, physical processes dominate. We do see significant oxygen summertime outgassing in the North KE and a small amount in the Central KE, consistent with summertime mixed layer production as well as solubility changes due to warming surface waters. If NCP were a significant component of the summertime air-sea oxygen budget in the North or Central KE regions, we would expect the loss of oxygen through calculated air-sea exchange to be greater than the observed water column oxygen loss and significant positive (net NCP) residuals in the summertime (Fig. 6). However, when integrated to the base of the wintertime mixed layer, the net residual is flat or negative, indicating that much or all of the mixed layer production is respired before it is exported from the upper ocean. An important point from these comparisons is that referring to organic carbon export from the upper ocean as NCP regardless of the depth or time of integration can create confusion about what pools and fluxes of organic matter production and respiration can or should be included in NCP or ANCP.

Palevsky and Quay (2017) calculate an annual net community production from repeat surface O_2/Ar measurements of 0.5 ± 0.7 mol C m^{-2} yr^{-1} over an area that partially covers our North KE region but extends further north into the subpolar gyre (Fig. D.1). While only using data from the surface ocean, this integration is over a similar spatial scale and is also integrated down to the base of the wintertime mixed layer and, importantly, over a similarly large spatial extent as the current study, making it the most applicable comparison and supporting our finding of little ANCP contribution to the annual oxygen and carbon budgets. However, while Palevsky and Quay (2017) find a small annual impact of ANCP on the column integrated oxygen and DIC budgets, in Palevsky et al. (2016) they do find significant spring and summer depth integrated net community production, which we do not see. Furthermore, despite the small impact of ANCP on the annual, column integrated oxygen or DIC budgets, Palevsky and Quay (2017) find that it is important to changes in the partial pressure of carbon dioxide and therefore the air-sea flux due to seasonal variations in the mixed layer depth. The study area of Palevsky et al. (2016) and Palevsky and Quay (2017) has only a small overlap with our Central KE region and therefore offers little insight into our net oxygen budget in that region.

In the South KE region, mode water is not formed and the residual oxygen is equivalent to biological production, yielding a net organic carbon production of 1.4 ± 1.5 mol C m^{-2} yr^{-1} (2.1 ± 2.2 mol O_2 m^{-2} yr^{-1} and a O:C of 1.45 (Hedges et al., 2002)). The variability observed in this region over the three years of our study (Fig. 6, Table 2) makes the three-year mean statistically indistinguishable from zero; however, in years two and three ANCP is significant and the magnitude is similar to two previous studies at S1. Honda et al. (2016) measured particulate organic carbon fluxes from drifting sediment traps over 2010–2012, yielding an ANCP of approximately 1.6 mol C m^{-2} yr^{-1} (average of 100 and 150 m trap data). In Wakita et al. (2016), ANCP of 2.8 ± 0.5 mol C m^{-2} yr^{-1} was calculated from a mass balance of

dissolved inorganic carbon down to the base of the wintertime mixed layer depth. Finally, a similar oxygen mass balance using three floats in the subtropical North Pacific just to the west of the South KE box determined an ANCP of 2–2.4 mol C m^{-2} yr^{-1} (Yang et al., 2017).

5. Conclusions

In the Kuroshio Extension region, the strong CO_2 flux into the ocean has been attributed to a tradeoff from a biologically dominated flux north of the Kuroshio Extension to a temperature dominated region south of the KE (Takahashi et al., 2002) and to a mixture of biology and geostrophic advection of DIC (Ayers and Lozier, 2012). In an effort to resolve the role of biological production in driving oceanic uptake of carbon dioxide in the Western North Pacific, we deployed 8 floats equipped with in situ calibrated oxygen sensors across the Kuroshio Extension. We divided float profiles into North, Central, and South Kuroshio Extension regions primarily through temperature and salinity relationships. Averaging of float measurements into three regions avoided the high advective fluxes that would result from floats crossing fronts and biogeochemical property boundaries over short time scales, which follows the findings of a recent carbon budget in the Southern Ocean from a state estimate model (Rosso et al., 2017). Interpretation of these data with an upper ocean model suggests that physical processes dominate the annual upper ocean oxygen budget in the North and Central regions, with biological processes most important in the South region (Fig. 8).

We found little evidence for a strong role of net biological production in the annual oxygen budget in the northern two regions. The North and particularly the Central region correspond to the transition zone north of the Kuroshio Extension and the main Kuroshio Extension, the area of strong CO_2 uptake by the ocean (Takahashi et al., 2009; Fig. 1). In both these regions we observed a strong annual oxygen flux into the ocean. Given that biological processes drive oxygen and inorganic carbon in opposite directions, the presence of both a strong oxygen uptake and strong carbon uptake suggests a physical explanation. Using the upper ocean box model to calculate the contribution of physical oxygen fluxes to the observed changes, the North and Central regions had residual oxygen fluxes of -5.4 ± 1.1 and -5.9 ± 0.1 mol O_2 m^{-2} yr^{-1}, respectively. These regions are areas of mode water formation and ventilation prior to subduction into the ocean interior. Plotting the isopycnal boundaries of Central Mode Water and Subtropical Mode Water over our three regions (Fig. 7) indicates that CMW outcrops in the North and subducts below the deepest mixed layers in the Central and South regions. STMW is formed and destroyed seasonally in the North, but outcrops in the Central region, before sliding below the deepest mixed layers of the South region. If the entire oxygen residual flux is due to the unaccounted for subduction of mode waters, we calculate mode water formation rates of 4.0 ± 0.9 and 7.6 ± 0.1 Sv of CMW and STMW, respectively.

These findings indicate a primarily physical control on the large-scale oxygen budget in the Western North Pacific north of ~ 32°N. It is likely that measurable ANCP and organic carbon production exist along the Kuroshio Extension in localized areas, but when integrated over the large spatial scales of the western North Pacific and annual time periods, this ANCP is swamped by a larger physical signal. Over large areas, the dominant uptake mechanism for oxygen is subduction of mode waters that are removed from contact with the atmosphere and we infer that this is an important mechanism in the net uptake of carbon dioxide in this region. This has broader implications for understanding the biological and physical controls on the upper ocean oxygen and carbon budgets, especially in similar Western Boundary Current regions. Both our current findings and where they add to previous work point toward the need to understand physical and biological processes through the full depth of the upper ocean. Horizontal transport is an important process throughout the upper water column and explicit parameterization of sub-mixed layer horizontal transport and lateral induction would allow the direct inclusion of mode water formation in models such as this. Pairing of large-scale observations of oxygen and, if possible, carbon parameters from autonomous vehicles would help to understand the exact relationship and timing between the biological and physical processes that set the air-sea fluxes of oxygen and carbon dioxide. Additionally, this would help to put the time series sites where much work has already been done in context with the broader region.

This method of interpretation yields lessons for future interpretation of biogeochemical Argo data:

1. The introduction of large apparent advective fluxes due to repeated crossings of fronts between water masses can be minimized in mass balance interpretations of upper ocean tracer data by averaging over large areas. This represents a tradeoff between representation of spatial heterogeneity with the ability to understand fluxes on an annual cycle. Similarly, uncertainty in air-sea fluxes is reduced by averaging multiple floats with independent oxygen sensors.
2. Fronts that fluctuate seasonally and interannually can make interpretation of data difficult using strict geographic boundaries. Interpretation of groups of floats through the separation of profiles into biogeographical regions that are defined through temperature, salinity, and biogeochemical properties accommodates these seasonally and interannually varying boundaries.

Acknowledgements

We would like to thank Stephen Riser and Dana Swift for their collaboration in SOS-Argo design, fabrication, and deployment. Rick Rupan and Dale Ripley constructed the SOS-Argo floats at the University of Washington float laboratory. The crew of the R/V Melville and the students of the 2013 UW undergraduate oceanography student cruise were of great help during float deployments in the Kuroshio Extension. SOS-Argo float measurements, including air-calibrated oxygen, are available at: https://sites.google.com/a/uw.edu/sosargo/home. The upper ocean mass balance model is available as a set of Matlab files upon request. Float development and deployments were supported by a National Science Foundation (NSF) grant OCE-1129112. S. Bushinsky was supported by an NSF Graduate Research Fellowship and an NSF IGERT training grant (#NSF1068839) while at the University of Washington and on the Southern Ocean Carbon and Climate Observations and Modeling (SOCCOM) NSF grant PLR-1425989 and the Carbon Mitigation Initiative (CMI) project sponsored by BP while at Princeton University. We would like to thank six anonymous reviewers for their detailed and insightful comments.

Appendix A. Float measurements

Float track, temperature (SST), oxygen supersaturation (ΔO_2), concentration, and mixed layer depth (MLD, magenta lines) are plotted for floats KE-1, 2, 4-8 (Fig. A.1). Floats are organized roughly from South-North, in order of float deployment. Supersaturation, concentration, temperature, and mixed layer depth follow seasonal cycles of warming waters in the spring-summer associated with increased supersaturation, decreased

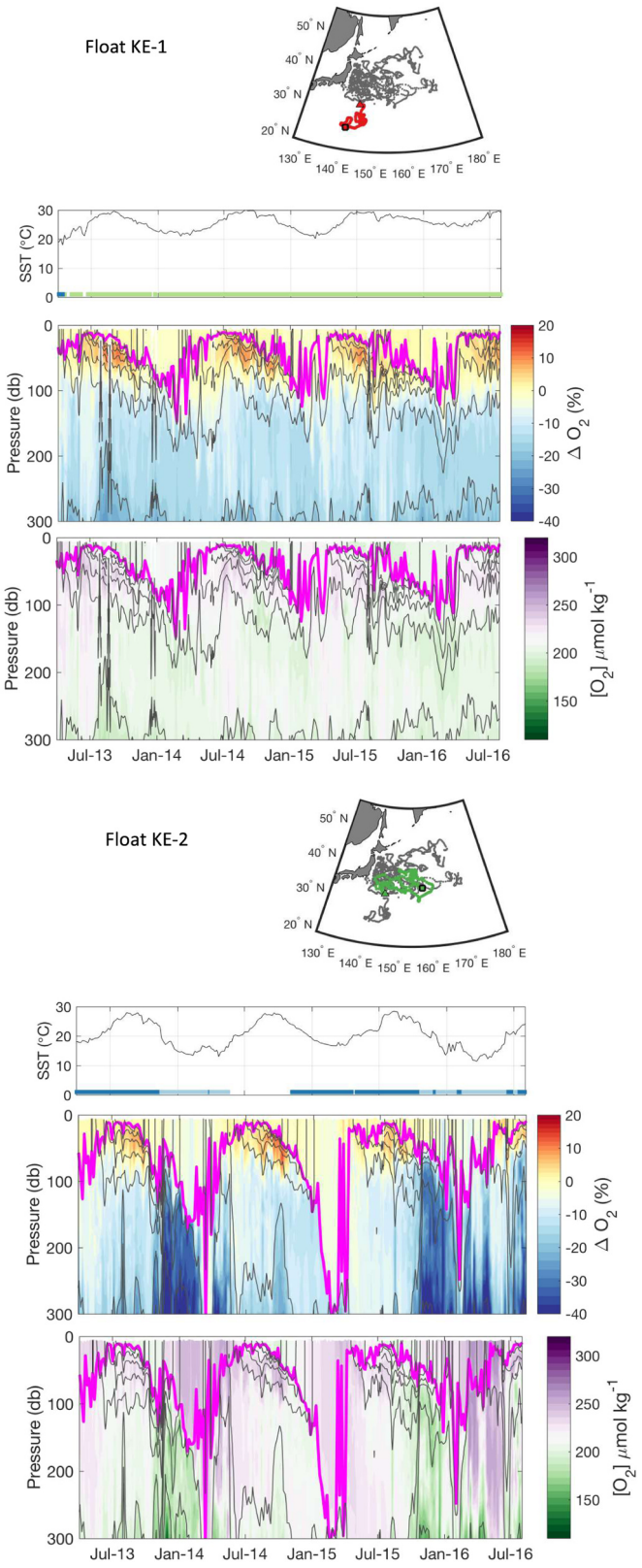

Fig. A.1. Individual float tracks, sea surface temperatures, upper ocean oxygen supersaturations, and concentrations are plotted for floats KE-1,2,4-8. The triangle represents initial float location. Plotted underneath the SST curves are colors that correspond to the region (if any) into which profile was placed (light blue: North, dark blue: Central, light green: South; regional definitions in Section 3.1 and Fig. 3).

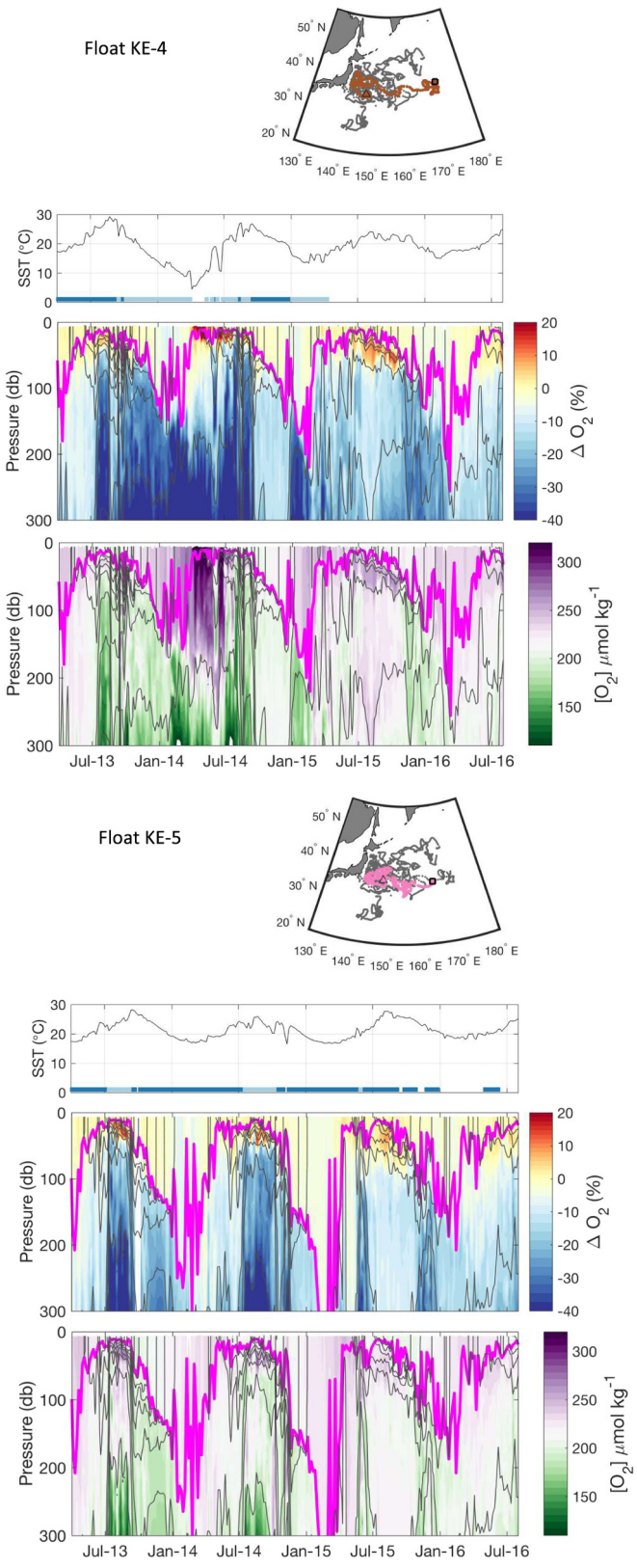

Fig. A.1. (*continued*)

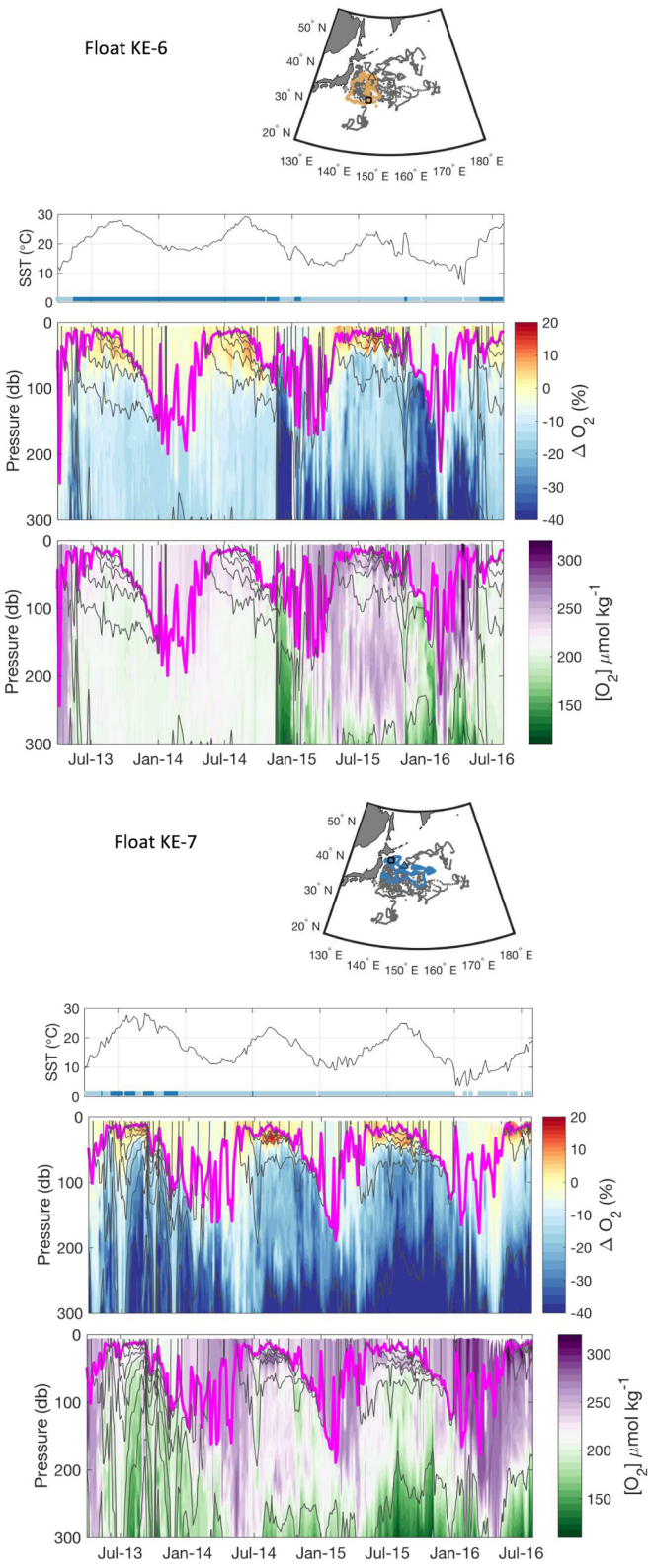

Fig. A.1. (*continued*)

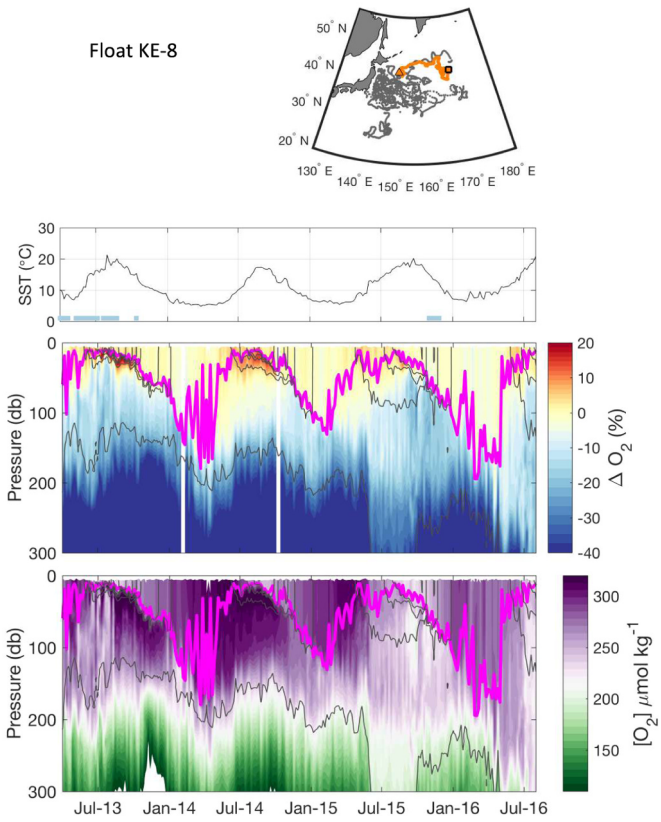

Fig. A.1. (*continued*)

solubility and concentration, and shallow mixed layer depths. From fall to winter mixed layer depths deepen and temperatures cool, increasing solubility and decreasing supersaturation.

Appendix B. Importance of the "cool-skin" effect on air-sea oxygen fluxes

To estimate the importance of the "cool-skin" effect on air-sea oxygen fluxes a wind-speed dependent temperature correction was calculated for both low-wind and high-wind speed cases (Alappattu et al., 2017):

$$\Delta T_{low} = A(U_{10})^2 + BU_{10} + C \tag{B.1}$$

$$\Delta T_{high} = DU_{10} + E \tag{B.2}$$

where ΔT_{low} is the temperature difference at wind speeds less than or equal to 4 m s^{-1}, ΔT_{high} is the temperature difference above 4 m s^{-1}, and A (0.035), B (-0.24), C (0.85), D (-0.0037) and E (0.35) are empirical constants fit to observations of the temperature differences between the ocean skin and the bulk mixed layer off the coast of North Carolina (Alappattu et al., 2017). The calculated temperature differences range from a ~ 0.8 °C cooler sea surface at low wind speeds to ~ 0.4 °C cooler at higher wind speeds. These equations do not account for the entire cool-skin effect, but are the majority of the signal and sufficient to determine whether the impact is important for air-sea oxygen fluxes.

The adjusted temperature was only applied to the diffusive component of the air-sea flux (F_S, Eq. (3)), under the assumption that bubbles injected into the ocean would experience an exchange temperature more similar to that of the bulk mixed layer. If we combine Eqs. (3) and (4),

$$F_S = 1.3\times10^{-4}U_a^*\left(\frac{S_{O2}}{660}\right)^{-0.5}\left([O_{2,sat}] - [O_2]\right)\frac{\rho_w}{10^6} \tag{B.3}$$

it becomes apparent that the cool-skin effect will be important in both the calculation of the temperature dependent Schmidt number (S_{O2}) and the saturation concentration of oxygen ($[O_{2,sat}]$). However, the relative temperature dependencies of the $\left(\frac{S_{O2}}{660}\right)^{-0.5}$ term and $[O_{2,sat}]$ are of approximately

equal magnitudes and opposite sign (Fig. B.1). This is similar to the relationship between the Schmidt number and solubility dependencies found in Woolf et al. (2016, Eq. (12) and (6) respectively). The end result is that the net impact on the air-sea flux is negligible (Fig. B.2) for oxygen. Therefore, these calculations were not included in the air-sea fluxes calculated in this study.

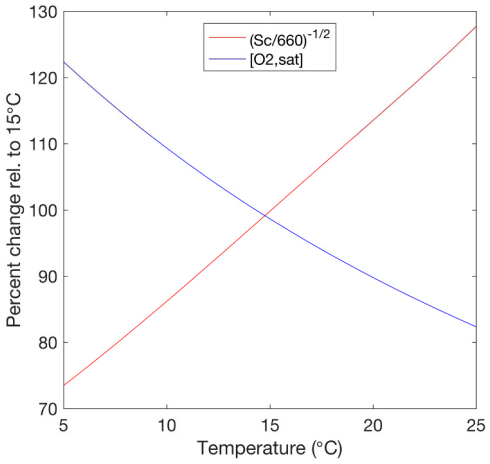

Fig. B.1. Temperature dependencies of the oxygen saturation concentration and the Schmidt number term $\left(\frac{S_{O2}}{660}\right)^{-0.5}$ of Eqs. (4) and (B.3). Salinity is constant at 35 and both terms are represented as a percentage relative to the value at 15 °C.

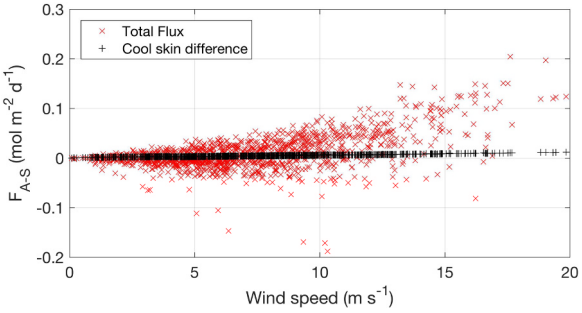

Fig. B.2. An example of the impact of the cool-skin effect on float 7665 (KE-7). The temperature difference due to the cool-skin effect was calculated from Eqs. (B.1) and (B.2). The difference due to the cool skin flux (black symbols, flux without the cool skin effect minus cool skin flux) and the total air-sea flux without the cool skin flux (red) are plotted as a function of wind speed.

Appendix C. Impact of uncertainty in oxygen measurements

To quantify the reduction in uncertainty in the air-sea flux of oxygen, we ran two Monte Carlo simulations: one with uncertainties derived from the air calibrations described in Bushinsky et al. (2016) and one with optode uncertainties set to ± 2%. Frequency histograms of individual flux components (F_S, F_P, and F_C) are plotted for each region in Fig. C1. Increased uncertainty in the oxygen measurement impacts F_S most strongly, followed by F_P. F_C is insensitive to the surface oxygen concentration and therefore does not increase in uncertainty.

The South region has the largest increase in $F_{A\text{-}S}$ uncertainty due to optode measurement uncertainty because the region only has data from one float and therefore there is no minimization of uncertainty through averaging of uncorrelated measurements.

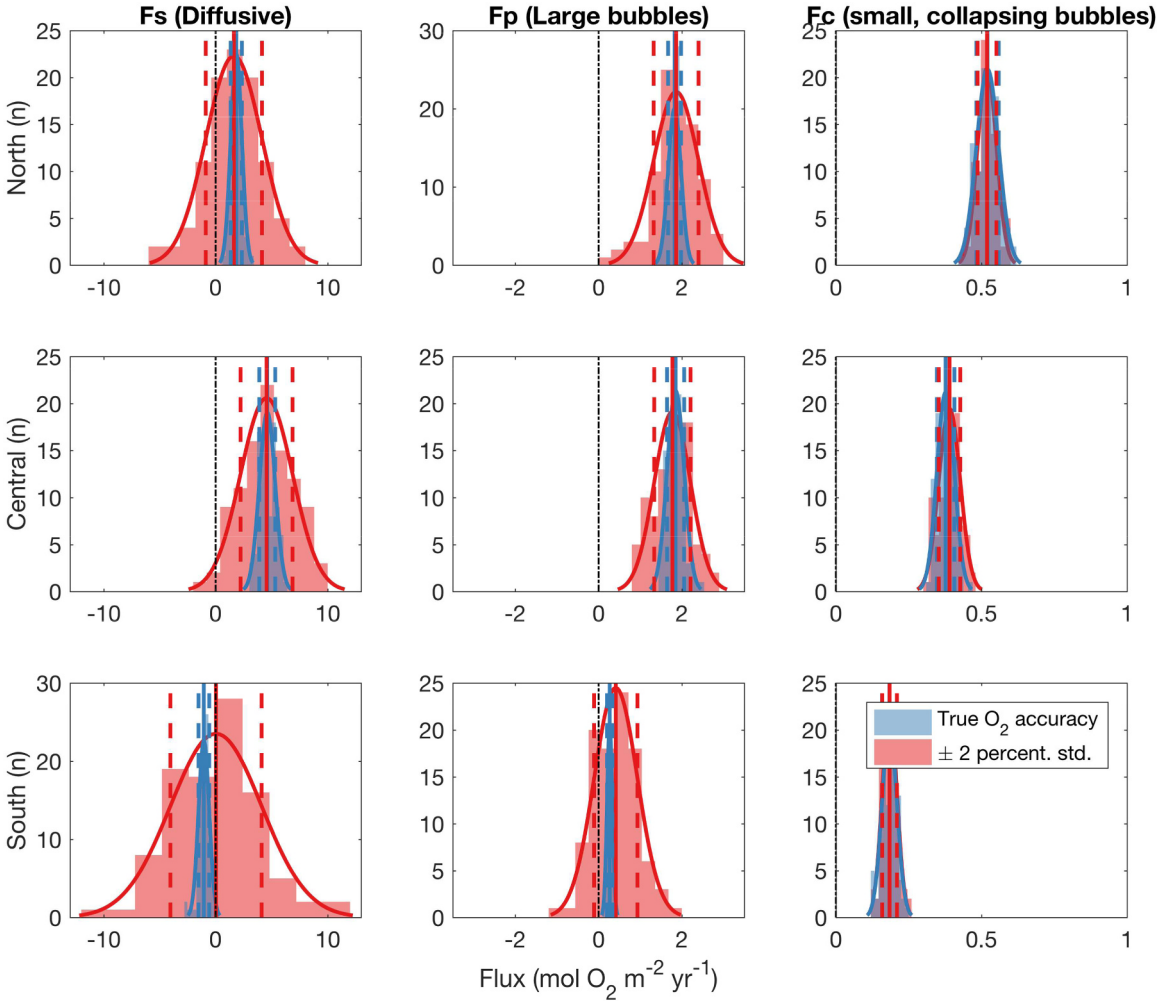

Fig. C.1. Monte Carlo uncertainties for $F_{A\text{-}S}$ component fluxes from the 2013–2014 model year for all three regions. Histogram areas represent the range of output from the Monte Carlo simulation. Solid lines represent a reference normal distribution based on the mean and standard deviation of the data. Dashed colored lines represent ± 1 s.d. for the histograms and the dash-dotted black line is 0 mol O_2 m^{-2} yr^{-1}.

Appendix D

To aid in comparison to prior studies, we have included Fig. D.1, which includes both the regions defined in this study as well as six time series site locations in the broader Kuroshio region: K1, K2, KNOT, K3, KEO, and S1, in addition to the boundary of the "Kuroshio region" from Palevsky et al. (2016).

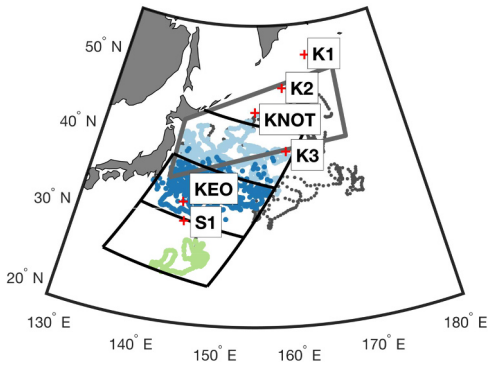

Fig. D.1. Regional boundaries from this region (black lines), time series site locations from prior studies (red +'s) and the regional boundaries from Palevsky et al. (2016) "Kuroshio region" (thick gray lines).

References

Alappattu, D.P., Wang, Q., Yamaguchi, R., Lind, R.J., Reynolds, M., Christman, A.J., 2017. Warm layer and cool skin corrections for bulk water temperature measurements for air-sea interaction studies. J. Geophys. Res. Ocean 122, 6470–6481. https://doi.org/10.1002/2017JC012688.

Ayers, J.M., Lozier, M.S., 2012. Unraveling dynamical controls on the North Pacific carbon sink. J. Geophys. Res. 117, C01017. https://doi.org/10.1029/2011JC007368.

Ayers, J.M., Lozier, M.S., 2010. Physical controls on the seasonal migration of the North Pacific transition zone chlorophyll front. J. Geophys. Res. Ocean 115, 1–11. https://doi.org/10.1029/2009JC005596.

Bentamy, A., Croize-Fillon, D., Perigaud, C., 2008. Characterization of ASCAT measurements based on buoy and QuikSCAT wind vector observations. Ocean Sci. 4, 265–274. https://doi.org/10.5194/os-4-265-2008.

Bittig, H.C., Körtzinger, A., 2016. Technical note: oxygen optodes on profiling platforms: update on response times, in-air measurements, and in-situ drift. Ocean Sci. Discuss. 1–15. https://doi.org/10.5194/os-2016-75.

Bittig, H.C., Körtzinger, A., 2015. Tackling oxygen optode drift: near-surface and in-air oxygen optode measurements on a float provide an accurate in-situ reference. J. Atmos. Ocean Technol. 32, 1536–1543. https://doi.org/10.1175/JTECH-D-14-00162.1.

Bittig, H.C., Körtzinger, A., Neill, C., van Ooijen, E., Plant, J.N., Hahn, J., Johnson, K.S., Yang, B., Emerson, S.R., 2017. Oxygen optode sensors: principle, characterization, calibration and application in the Ocean. Front. Mar. Sci. https://doi.org/10.3389/fmars.2017.00429.

Bograd, S.J., Foley, D.G., Schwing, F.B., Wilson, C., Laurs, R.M., Polovina, J.J., Howell, E.A., Brainard, R.E., 2004. On the seasonal and interannual migrations of the transition zone chlorophyll front. Geophys. Res. Lett. 31, 1–5. https://doi.org/10.1029/2004GL020637.

Bushinsky, S.M., Emerson, S., 2013. A method for in-situ calibration of aanderaa oxygen sensors on surface moorings. Mar. Chem. 155, 22–28. https://doi.org/10.1016/j.marchem.2013.05.001.

Bushinsky, S.M., Emerson, S.R., 2015. Marine biological production from in situ oxygen measurements on a profiling float in the subarctic Pacific Ocean. Glob. Biogeochem. Cycles 29. https://doi.org/10.1002/2015GB005251.

Bushinsky, S.M., Emerson, S.R., Riser, S.C., Swift, D.D., 2016. Accurate oxygen measurements on modified Argo floats using in situ air calibrations. Limnol. Oceanogr. Methods 00, 1–48. https://doi.org/10.1002/lom3.10107.

Bushinsky, S.M., Gray, A.R., Johnson, K.S., Sarmiento, J.L., 2017. Oxygen in the Southern Ocean from Argo floats: determination of processes driving air-sea fluxes. J. Geophys. Res. Ocean 122. https://doi.org/10.1002/2017JC012923.

Chierici, M., Fransson, A., Nojiri, Y., 2006. Biogeochemical processes as drivers of surface fCO2 in contrasting provinces in the subarctic North Pacific Ocean. Glob. Biogeochem. Cycles 20, 1–16. https://doi.org/10.1029/2004GB002356.

Cronin, M.F., Pelland, N., Emerson, S., Crawford, W.R., 2015. Estimating diffusivity from the mixed layer heat and salt balances in the North Pacific. J. Geophys. Res. Ocean 120, 7346–7362. https://doi.org/10.1002/2015JC011010.Received.

D'Asaro, E.A., McNeil, C., 2013. Calibration and stability of oxygen sensors on autonomous floats. J. Atmos. Ocean Technol. 30, 1896–1906. https://doi.org/10.1175/JTECH-D-12-00222.1.

de Boyer Montégut, C., Madec, G., Fischer, A.S., Lazar, A., Iudicone, D., 2004. Mixed layer depth over the global ocean: an examination of profile data and a profile-based climatology. J. Geophys. Res. 109, C12003. https://doi.org/10.1029/2004JC002378.

Drucker, R., Riser, S.C., 2016. In situ phase-domain calibration of oxygen Optodes on profiling floats. Methods Oceanogr. 17, 296–318. https://doi.org/10.1016/j.mio.2016.09.007.

Emerson, S., Bushinsky, S., 2014. Oxygen concentrations and biological fluxes in the open ocean. Oceanography 27, 168–171. https://doi.org/10.5670/oceanog.2014.20.

Emerson, S., Stump, C., 2010. Net biological oxygen production in the ocean—II: remote in situ measurements of O2 and N2 in subarctic pacific surface waters. Deep Sea Res. Part I Oceanogr. Res. Pap. 57, 1255–1265. https://doi.org/10.1016/j.dsr.2010.06.001.

Emerson, S., Stump, C., Nicholson, D., 2008. Net biological oxygen production in the ocean: remote in situ measurements of O2 and N2 in surface waters. Glob. Biogeochem. Cycles 22, GB3023. https://doi.org/10.1029/2007GB003095.

Emerson, S.R., Bushinsky, S., 2016. The role of bubbles during air-sea gas exchange. J. Geophys. Res. Ocean 121, 4360–4376. https://doi.org/10.1002/2016JC011744.

Fassbender, A.J., Sabine, C.L., Cronin, M.F., Sutton, A.J., 2017. Mixed layer carbon cycling at the Kuroshio Extension Observatory. Glob. Biogeochem. Cycles 1–17. https://doi.org/10.1002/2016GB005547.

Gruber, N., Doney, S.C., Emerson, S.R., Gilbert, D., Kobayashi, T., Körtzinger, A., Johnson, G.C., Johnson, K.S., Riser, S.C., Ulloa, O., 2009. Adding oxygen to Argo: developing a global in-situ observatory for ocean deoxygenation and biogeochemistry. OceanObs 09.

Hansell, D.A., Carlson, C.A., 2002. Dissolved organic carbon export with North Pacific Intermediate Water formation. Glob. Biogeochem. Cycles 16.

Hansell, D.A., Carlson, C.A., 2001. Marine dissolved organic matter and the carbon cycle. Oceanography 14, 41–49.

Hardman-Mountford, N.J., Hirata, T., Richardson, K.A., Aiken, J., 2008. An objective methodology for the classification of ecological pattern into biomes and provinces for the pelagic ocean. Remote Sens. Environ. 112, 3341–3352. https://doi.org/10.1016/j.rse.2008.02.016.

Harrison, P.J., Whitney, F.A., Tsuda, A., Saito, H., Tadokoro, K., 2004. Nutrient and plankton dynamics in the NE and NW Gyres of the subarctic Pacific Ocean. J. Oceanogr. 60, 93–117. https://doi.org/10.1023/B:JOCE.0000038321.57391.2a.

Hartmann, D.L., 1994. The ocean general circulation and climate. In: Hartmann, D.L. (Ed.), Global Physical Climatology. Academic Press, San Diego, pp. 171–203.

Hasse, L., 1971. The sea surface temperature deviation and heat flow at the sea-air interface. Bound.-Layer Meteorol. 1, 368–379. https://doi.org/10.1007/BF02186037.

Hayward, T.L., 1997. Pacific Ocean climate change: atmospheric forcing, ocean circulation and ecosystem response. Trends Ecol. Evol. 12, 150–154.

Hedges, J.I., Baldock, J.A., Gélinas, Y., Lee, C., Peterson, M.L., Wakeham, S.G., 2002. The biochemical and elemental compositions of marine plankton: a NMR perspective. Mar. Chem. 78, 47–63. https://doi.org/10.1016/S0304-4203(02)00009-9.

Hofmann, M., Schellnhuber, H., 2009. Oceanic acidification affects marine carbon pump and triggers extended marine oxygen holes. Proc. Natl. Acad. Sci. 106, 3017–3022. https://doi.org/10.1073/pnas.0813384106.

Honda, M.C., Kawakami, H., Matsumoto, K., Wakita, M., Fujiki, T., Mino, Y., Sukigara, C., Kobari, T., Uchimiya, M., Kaneko, R., Saino, T., 2016. Comparison of sinking particles in the upper 200 m between subarctic station K2 and subtropical station S1 based on drifting sediment trap experiments. J. Oceanogr. 72, 373–386. https://doi.org/10.1007/s10872-015-0280-x.

Inoue, R., Honda, M.C., Fujiki, T., Matsumoto, K., Kouketsu, S., Suga, T., Saino, T., 2016a. Western North Pacific integrated physical-biogeochemical ocean observation experiment (INBOX): Part 2. Biogeochemical responses to eddies and typhoons revealed from the S1 mooring and shipboard measurements. J. Mar. Res. 74, 71–99. https://doi.org/10.1357/002224016819257335.

Inoue, R., Suga, T., Kouketsu, S., Kita, T., Hosoda, S., Kobayashi, T., Sato, K., Nakajima, H., Kawano, T., 2016b. Western North Pacific integrated physical-biogeochemical ocean observation experiment (INBOX): Part 1. Specifications and chronology of the S1-INBOX floats. J. Mar. Res. 74, 43–69. https://doi.org/10.1357/002224016819257344.

Jayne, S.R., Hogg, N.G., Waterman, S.N., Rainville, L., Donohue, K.A., Randolph Watts, D., Tracey, K.L., McClean, J.L., Maltrud, M.E., Qiu, B., Chen, S., Hacker, P., 2009. The Kuroshio extension and its recirculation gyres. Deep. Res. Part I Oceanogr. Res. Pap. 56, 2088–2099. https://doi.org/10.1016/j.dsr.2009.08.006.

Johnson, K.S., Plant, J.N., Coletti, L.J., Jannasch, H.W., Sakamoto, C.M., Riser, S.C., Swift, D.D., Williams, N.L., Boss, E., Haëntjens, N., Talley, L.D., Sarmiento, J.L., 2017. Biogeochemical sensor performance in the SOCCOM profiling float array. J. Geophys. Res. Ocean. 2–36. https://doi.org/10.1002/2017JC012838.

Johnson, K.S., Plant, J.N., Riser, S.C., Gilbert, D., 2015. Air oxygen calibration of oxygen optodes on a profiling float array. J. Atmos. Ocean Technol. 32, 2160–2172. https://doi.org/10.1175/JTECH-D-15-0101.1.

Liang, J.-H., Deutsch, C., McWilliams, J.C., Baschek, B., Sullivan, P.P., Chiba, D., 2013. Parameterizing bubble-mediated air-sea gas exchange and its effect on ocean ventilation. Glob. Biogeochem. Cycles 27, 894–905. https://doi.org/10.1002/gbc.20080.

Longhurst, A., Sathyendranath, S., Platt, T., Caverhill, C., 1995. An estimate of global primary production in the ocean from satellite radiometer data. J. Plankton Res. 17, 1245–1271. https://doi.org/10.1093/plankt/17.6.1245.

Nicholson, D., Emerson, S., Eriksen, C.C., 2008. Net community production in the deep euphotic zone of the subtropical North Pacific gyre from glider surveys. Limnol. Oceanogr. 53, 2226–2236. https://doi.org/10.4319/lo.2008.53.5_part_2.2226.

Oka, E., Qiu, B., Takatani, Y., Enyo, K., Sasano, D., Kosugi, N., Ishii, M., Nakano, T., Suga, T., 2015. Decadal variability of Subtropical Mode Water subduction and its impact on biogeochemistry. J. Oceanogr. 71, 389–400. https://doi.org/10.1007/s10872-015-0300-x.

Palevsky, H.I., Quay, P.D., 2017. Influence of biological carbon export on ocean carbon uptake over the annual cycle across the North Pacific Ocean. Glob. Biogeochem. Cycles 31, 81–95. https://doi.org/10.1002/2016GB005527.

Palevsky, H.I., Quay, P.D., Lockwood, D.E., Nicholson, D.P., 2016. The annual cycle of gross primary production, net community production, and export efficiency across the North Pacific Ocean. Glob. Biogeochem. Cycles 30, 361–380. https://doi.org/10.1002/2015GB005318.

Plant, J.N., Johnson, K.S., Sakamoto, C.M., Jannasch, H.W., Coletti, L.J., Riser, S.C., Swift, D.D., 2016. Net community production at Ocean Station Papa observed with nitrate and oxygen sensors on profiling floats. Glob. Biogeochem. Cycles 30, 859–879. https://doi.org/10.1002/2015GB005349.

Qiu, B., Chen, S., 2005. Variability of the Kuroshio Extension jet, recirculation gyre , and mesoscale eddies on decadal time scales. J. Phys. Oceanogr. 35, 2090–2103. https://doi.org/10.1175/JPO2807.1.

Qiu, B., Chen, S., Schneider, N., 2017. Dynamical links between the decadal variability of the Oyashio and Kuroshio Extensions. J. Clim. 30, 9591–9605. https://doi.org/10.1175/JCLI-D-17-0397.1.

Roden, G.I., 1991. Subarctic-Subtropical Transition Zone of the North Pacific: Large-Scale Aspects and Mesoscale Structure, NOAA Technical Report: Biology, Oceanography, and Fisheries of the North Pacific Transition Zone and Subarctic Frontal Zone.

Rosso, I., Mazloff, M.R., Verdy, A., Talley, L.D., 2017. Space and time variability of the Southern Ocean carbon budget. J. Geophys. Res. Ocean 122, 7407–7432. https://doi.org/10.1002/ 2016JC012646.

Suga, T., Aoki, Y., Saito, H., Hanawa, K., 2008. Ventilation of the North Pacific subtropical pycnocline and mode water formation. Prog. Oceanogr. 77, 285–297. https://doi.org/10.1016/j.pocean.2006.12.005.

Suga, T., Motoki, K., Aoki, Y., Macdonald, A.M., 2004. The North Pacific climatology of winter mixed layer and mode waters. J. Phys. Oceanogr. 34, 3–22. https://doi.org/10.1175/1520-0485(2004)034<0003:TNPCOW>2.0.CO;2.

Sun, O.M., Jayne, S.R., Polzin, K.L., Rahter, B.A., Laurent St., L.C., 2013. Scaling turbulent dissipation in the transition layer. J. Phys. Oceanogr. 43, 2475–2489. https://doi.org/10.1175/JPO-D-13-057.1.

Takahashi, T., Sutherland, S.C., Sweeney, C., Poisson, A., Metzl, N., Tilbrook, B., Bates,

N., Wanninkhof, R., Feely, R.A., Sabine, C., Olafsson, J., Nojiri, Y., 2002. Global sea-air CO_2 flux based on climatological surface ocean pCO_2, and seasonal biological and temperature effects. Deep. Res. Part II Top. Stud. Oceanogr. 49, 1601–1622. https://doi.org/10.1016/S0967-0645(02)00003-6.

Takahashi, T., Sutherland, S.C., Wanninkhof, R., Sweeney, C., Feely, R.A., Chipman, D.W., Hales, B., Friederich, G., Chavez, F., Sabine, C., Watson, A., Bakker, D.C.E., Schuster, U., Metzl, N., Yoshikawa-Inoue, H., Ishii, M., Midorikawa, T., Nojiri, Y., Körtzinger, A., Steinhoff, T., Hoppema, M., Olafsson, J., Arnarson, T.S., Tilbrook, B., Johannessen, T., Olsen, A., Bellerby, R., Wong, C.S., Delille, B., Bates, N.R., de Baar, H.J.W., 2009. Climatological mean and decadal change in surface ocean pCO_2, and net sea-air CO_2 flux over the global oceans. Deep Res. Part II Top. Stud. Oceanogr. 56, 554–577. https://doi.org/10.1016/j.dsr2.2008.12.009.

Takeshita, Y., Martz, T.R., Johnson, K.S., Plant, J.N., Gilbert, D., Riser, S.C., Neill, C., Tilbrook, B., 2013. A climatology-based quality control procedure for profiling float oxygen data. J. Geophys. Res. Ocean 118, 5640–5650. https://doi.org/10.1002/jgrc.20399.

Toggweiler, J.R., Sarmiento, J.L., 1985. Glacial to interglacial changes in atmospheric carbon dioxide: the critical role of ocean surface water in high latitudes. In: Sundquist, E.T., Broecker, W.S. (Eds.), The Carbon Cycle and Atmospheric CO_2: Natural Variations Archean to Present. American Geophysical Union, Washington, D. C, pp. 163–184.

Hoffert, Volk, 1985. The Carbon Cycle and Atmospheric CO_2: Natural Variations Archean to Present, Geophysical Monograph Series. American Geophysical Union, Washington, D.C. https://doi.org/10.1029/GM032.

Wakita, M., Honda, M.C., Matsumoto, K., Fujiki, T., Kawakami, H., Yasunaka, S., Sasai, Y., Sukigara, C., Uchimiya, M., Kitamura, M., Kobari, T., Mino, Y., Nagano, A., Watanabe, S., Saino, T., 2016. Biological organic carbon export estimated from the annual carbon budget observed in the surface waters of the western subarctic and subtropical North Pacific Ocean from 2004 to 2013. J. Oceanogr. 72, 665–685. https://doi.org/10.1007/s10872-016-0379-8.

Whalen, C.B., Talley, L.D., MacKinnon, J.A., 2012. Spatial and temporal variability of global ocean mixing inferred from Argo profiles. Geophys. Res. Lett. 39, L18612. https://doi.org/10.1029/2012GL053196.

Wolf, M.K., Hamme, R.C., Gilbert, D., Yashayaev, I., Thierry, V., 2018. Oxygen saturation surrounding deep-water formation events in the Labrador Sea from Argo-O2 data. Glob. Biogeochem. Cycles TBD. https://doi.org/10.1002/2017GB005829.

Wong, C., Waser, N.A., Nojiri, Y., Whitney, F., Page, J., Zeng, J., 2002. Seasonal cycles of nutrients and dissolved inorganic carbon at high and mid latitudes in the North Pacific Ocean during the Skaugran cruises: determination of new production and nutrient uptake ratios. Deep Sea Res. Part II Top. Stud. Oceanogr. 49, 5317–5338. https://doi.org/10.1016/S0967-0645(02)00193-5.

Woolf, D.K., Land, P.E., Shutler, J.D., Goddijn-Murphy, L.M., Donlon, C.J., 2016. On the calculation of air-sea fluxes of CO_2 in the presence of temperature and salinity gradients. J. Geophys. Res. Ocean 121, 1229–1248. https://doi.org/10.1002/2015JC011427.

Yang, B., Emerson, S.R., Bushinsky, S.M., 2017. Annual net community production in the subtropical Pacific Ocean from in-situ oxygen measurements on profiling floats. Glob. Biogeochem. Cycles 31, 728–744. https://doi.org/10.1002/2016GB005545.

Yasunaka, S., Nojiri, Y., Nakaoka, S.I., Ono, T., Mukai, H., Usui, N., 2013. Monthly maps of sea surface dissolved inorganic carbon in the North Pacific: basin-wide distribution and seasonal variation. J. Geophys. Res. Ocean 118, 3843–3850. https://doi.org/10.1002/jgrc.20279.